Dam Operations and Subsurface Hydrogeology Control Dynamics of Hydrologic Exchange Flows in a Regulated River Reach

Pin Shuai[1], Xingyuan Chen[1], Xuehang Song[1], Glenn Hammond[2], John Zachara[1], Patrick Royer[1], Huiying Ren[1], William Perkins[1], Marshall Richmond[1], and Maoyi Huang[1]

[1]Pacific Northwest National Laboratory
[2]Sandia National Laboratories

November 23, 2022

Abstract

Hydrologic exchange flows (HEFs) across the river-aquifer interface have important implications for biogeochemical processes and contaminant plume migration in the river corridor, yet little is known about the hydrogeomorphic factors that control HEFs dynamics under dynamic flow conditions. Here, we developed a 3-D numerical model for a large regulated river corridor along the Columbia River to study how HEFs are controlled by the interplays between dam-regulated flow conditions and hydrogeomorphic features of such river corridor system. Our results revealed highly variable intra-annual spatiotemporal patterns in HEFs along the 75-km river reach, as well as strong interannual variability with larger exchange volumes in wet years than dry years. In general, the river was losing during late spring to early summer when the river stage was high, and river was gaining in fall and winter when river stage was low. The magnitude and timing of river stage fluctuations controlled the timing of high exchange rates. Both river channel geomorphology and the thickness of a highly permeable river bank geologic layer controlled the locations of exchange hot spots, while the latter played a dominant role. Dam-induced, sub-daily to daily river stage fluctuations drove high-frequency variations in HEFs across the river-aquifer interfaces, resulting in greater overall exchange volumes as compared to the case without high-frequency flows. Our results demonstrated that upstream dam operations enhanced the exchange between river water and groundwater with strong potential influence on the associated biogeochemical processes and on the fate and transport of groundwater contaminant plumes in such river corridors.

Dam Operations and Subsurface Hydrogeology Control Dynamics of Hydrologic Exchange Flows in a Regulated River Reach

Pin Shuai[1*], Xingyuan Chen[1], Xuehang Song[1], Glenn E. Hammond[2], John Zachara[1], Patrick Royer[1], Huiying Ren[1], William A. Perkins[1], Marshall C. Richmond[1], and Maoyi Huang[1]

[1]Pacific Northwest National Laboratory, Richland, Washington, USA

[2]Sandia National Laboratories, Albuquerque, New Mexico, USA

*Corresponding author: Pin Shuai (Pin.Shuai@pnnl.gov)

Key Points:

- Hydrologic exchange flows across the riverbed show strong intra-annual spatiotemporal patterns as well as interannual variabilities
- Hot moments of HEFs are controlled by magnitude and timing of river stage fluctuations
- Hot spots of HEFs are primarily controlled by the thickness of the underlying highly permeable sediment layer

Abstract

Hydrologic exchange flows (HEFs) across the river-aquifer interface have important implications for biogeochemical processes and contaminant plume migration in the river corridor, yet little is known about the hydrogeomorphic factors that control HEFs dynamics under dynamic flow conditions. Here, we developed a 3-D numerical model for a large regulated river corridor along the Columbia River to study how HEFs are controlled by the interplays between dam-regulated flow conditions and hydrogeomorphic features of such river corridor system. Our results revealed highly variable intra-annual spatiotemporal patterns in HEFs along the 75-km river reach, as well as strong interannual variability with larger exchange volumes in wet years than dry years. In general, the river was losing during late spring to early summer when the river stage was high, and river was gaining in fall and winter when river stage was low. The magnitude and timing of river stage fluctuations controlled the timing of high exchange rates. Both river channel geomorphology and the thickness of a highly permeable river bank geologic layer controlled the locations of exchange hot spots, while the latter played a dominant role. Dam-induced, sub-daily to daily river stage fluctuations drove high-frequency variations in HEFs across the river-aquifer interfaces, resulting in greater overall exchange volumes as compared to the case without high-frequency flows. Our results demonstrated that upstream dam operations enhanced the exchange between river water and groundwater with strong potential influence on the associated biogeochemical processes and on the fate and transport of groundwater contaminant plumes in such river corridors.

Plain Language Summary

River stage fluctuations due to upstream dam operations enhance water exchange between rivers and aquifers. These exchange flows can stimulate biogeochemical processes in the subsurface. Here, we developed a 3-D numerical model to simulate the flow and transport in a flood plain aquifer within the free-flowing Columbia River corridor. Our simulations revealed large spatial and temporal variability in exchange flow magnitude and direction in response to different river flow conditions. Furthermore, river channel morphology and subsurface geology together controlled the locations of high exchange flow rates. Our study provides important insights on the behavior of groundwater contaminant plumes in the river corridors of large regulated river systems.

1. Introduction

Hydrologic exchange flows (HEFs) play a critical role in river corridor biogeochemical and ecological functions. They are broadly defined as all lateral and vertical water exchanges between the river channel and the adjacent subsurface, including hyporheic exchange, bank storage and overbank flows (Harvey & Gooseff, 2015). Exchange flows increase the contact between river water and subsurface sediments, and enhance the mixing of river water and groundwater which may each display unique geochemical and microbiological characteristics. Consequences can include stimulating biogeochemical reactions and the mobilization and transformation of contaminants and nutrients along the river corridor.

HEFs are controlled by the permeability of riverbed alluvium and associated aquifer sediments as well as the hydraulic gradient along the flow direction. Under constant flow condition, hydraulic gradient is static and controlled by channel and riverbed morphology such as pool and riffle sequence, riverbed meanders, point bars and bedforms (Boano et al., 2006; Cardenas et al., 2008; Cardenas, 2008; Stonedahl et al., 2013; Tonina & Buffington, 2007). Natural flow events (i.e. snowmelt, rainfall, and tides) and human perturbations (i.e. dam operations, groundwater pumping etc.) may induce river stage fluctuations that can drive temporal variations in hydraulic gradient and consequently change the magnitude and directions of HEFs in the river corridor (Song et al., 2018). River stage fluctuations could increase exchange volume of HEFs, and create hot spots and hot moments for biogeochemical reactions (Dwivedi et al., 2018; Gu et al., 2012; Shuai et al., 2017; Song et al., 2018). For example, river fluctuations driven by hydropeaking or tidal pumping enhance the exchange of dissolved oxygen (Musial et al., 2016), accelerate nitrogen cycling (Knights et al., 2017; Shuai et al., 2017), regulate hyporheic thermal regimes (Song et al., 2018), influence heavy metal attenuation (Zachara et al., 2016), and stimulate microbial activities in the hyporheic zone (Stegen et al., 2016). Studies under dynamic flow conditions have explored its effects on hyporheic exchange and biogeochemical activity (Gomez-Velez et al., 2017; Gu et al., 2012; Malzone et al., 2016; Schmadel et al., 2016; Shuai et al., 2017).

Hydrologic exchange has generally been evaluated at relatively small spatial scales ranging from cm's to 100s of meter under steady-state or base flow conditions (Cook et al., 2006; Hester, 2014; Ward et al., 2013; Zarnetske et al., 2011, 2012). In addition, research based on two-dimensional cross sections of riverbed or river banks have ignored the effects of complex pressure gradients induced by three-dimensional channel morphology or subsurface topography on HEFs. For example, hyporheic exchange was found to be sensitive to bedform steepness and lateral elongation by modeling flow in hundreds of complex synthetic three-dimensional (3-D) bedforms (Chen et al., 2018). A set of laboratory flume experiments associated with 3-D computational fluid dynamic (CFD) modeling revealed that the 3-D morphology of pool-riffle sequence was a primary control on surface flow and hyporheic exchange (Tonina & Buffington, 2007). More recently, subsurface structure such as the thickness of riverbed alluvial layer and underlying permeable layer was shown to control exchange flux magnitude for a downstream segment of Hanford Reach using a 3-D surface and subsurface CFD model (Bao et al., 2018a).

The cumulative effects and interactions of small-scale physical and biogeochemical processes associated with HEFs at ecologically relevant scales including river reaches or watersheds are not well understood (Harvey & Gooseff, 2015). Numerical models have become important tools for reach- and watershed-scale investigations of HEFs to alleviate the extensive effort and expense required to characterize and understand large river corridor systems (Gomez-

Velez et al., 2015; Kasahara & Wondzell, 2003; Kiel & Cardenas, 2014). Three main modeling approaches have been used to simulate river corridor hydrological processes: (1) empirical upscaling, (2) reduced-complexity modeling, and (3) distributed modeling (Ward et al., 2018). Empirical upscaling translates local-scale understanding of hydrological processes to the reach and watershed scales using empirical relationship based on field experiments or modeling studies (Gomez-Velez et al., 2015; Gomez-Velez & Harvey, 2014; Kiel & Cardenas, 2014; Marzadri et al., 2014). However, empirical models generally assume steady river discharge, and thus ignore the dynamic interactions between hydrologic forcing and geologic settings. Reduced-complexity models provide a mechanistic understanding of the most important processes including the dynamic hydrologic forcing, but they selectively omit or simplify other hydrologic processes perceived to be unimportant (Ward et al., 2018). One of the most widely used reduced-complexity models is the transient storage model that estimates advection, dispersion and transient storage at the reach (Bencala & Walters, 1983). On the other hand, distributed models allow a comprehensive representation of hydrological processes associated with the HEFs in a river corridor considering multiple geomorphic features and dynamic river flow conditions, despite the fact that they are more data intensive and computationally expensive.

In this study, we adopted a fully distributed modeling approach to investigate hydrologic exchange in a large, dynamic river corridor along an extended, free flowing reach of the Columbia River (the 75-km Hanford Reach). The Hanford Reach is bounded by large hydroelectric dams on its upstream and downstream ends. A 3-D groundwater flow and transport model was developed to simulate HEFs for the entire reach with complex hydromorphic and hydrogeologic features under dynamic flow conditions for a multiple-year time period that encompassed both wet and dry years. Our heuristic objectives were: (1) to evaluate the effects of river stage fluctuations, channel morphology and subsurface hydrogeology on the spatiotemporal patterns of HEFs across the river-aquifer interface; (2) to show the cumulative effects of local-scale hydrological processes over the entire river reach; and (3) to infer the role of high-frequency river stage fluctuations induced by dam operations on HEFs and the fate of nutrients and contaminants in the river corridor. Our study improves understanding of the critical roles that climate and river management operations play on HEFs across river-aquifer-terrestrial continuum that encompasses multiple geologic, geomorphic and hydrogeologic features under dynamic hydrologic conditions.

2. Materials and Methods

2.1 Study Site

Our study was conducted along the Hanford Reach of the Columbia River, a 75-km free flowing river stretch that is located within the Pasco Basin in south-central Washington State (Figure 1). The east side of the river is dominated by irrigated agricultural lands and west side of the river is predominantly dryland. The climate is arid to semi-arid with an average annual precipitation less than 180 mm (Gee et al., 2007).

The river corridor contains an unconfined aquifer that is hydrologically connected to the river. The unconfined aquifer consists of two major geologic units: the Hanford Formation (Hf) comprised of Pleistocene-age flood deposits and the underlying Ringold Formation with fluvio-lacustrine deposits of Miocene-Pliocene age (Thorne, 2004; Thorne et al., 2006). The Ringold Formation can be divided into four textural sub-units: Ringold E (Re) with coarser texture;

Ringold Taylor Flats (Rtf), Ringold Lower Mud (Rlm) and Ringold A (Ra) (see stratigraphy in Supplementary Information Figure S1). In some areas, the Cold Creek (Cc) unit exists between the Hanford and Ringold Formations. Underlying the entire basin is the Columbia River Basalt Group forming confining units at depth. The most permeable unit is Hf, followed by Cc and Ringold units (i.e., Re, Rtf, Rlm and Ra). The basalt unit exhibits low permeability except along interbeds; it is considered impermeable for the model calculations performed herein. The porosity and hydraulic conductivity for each geologic unit is summarized in Table 1.

All geologic units are not ubiquitous at the site and vary in topography. Most of the land surface is relatively flat, although the northern boundary is bordered by the Saddle Mountains with peak elevation of ~ 800 m and southwest portion of the site is bordered by the Rattlesnake Hills which rises to an elevation of ~ 1000 m. Basalt outcroppings in the Hanford 200 Area (at the center portion of the Hanford site on the west side of the river) form the Gable Mountain and the Gable Butte with a peak elevation of ~350 m and ~240 m, respectively. The thickness of Hanford unit at the top of the unconfined aquifer within study domain ranges from 0 to 56 m (Figure 2), with a paleochannel filled with Hanford gravel located near the upstream area. The thickness of the vadose zone ranges from less than10 m near the Columbia River to ~ 100 m in the Hanford 200 Area plateau (Murphy et al., 1996). Riverbed sediment is mostly gravel with grain size ranging from few centi-meters to several meters.

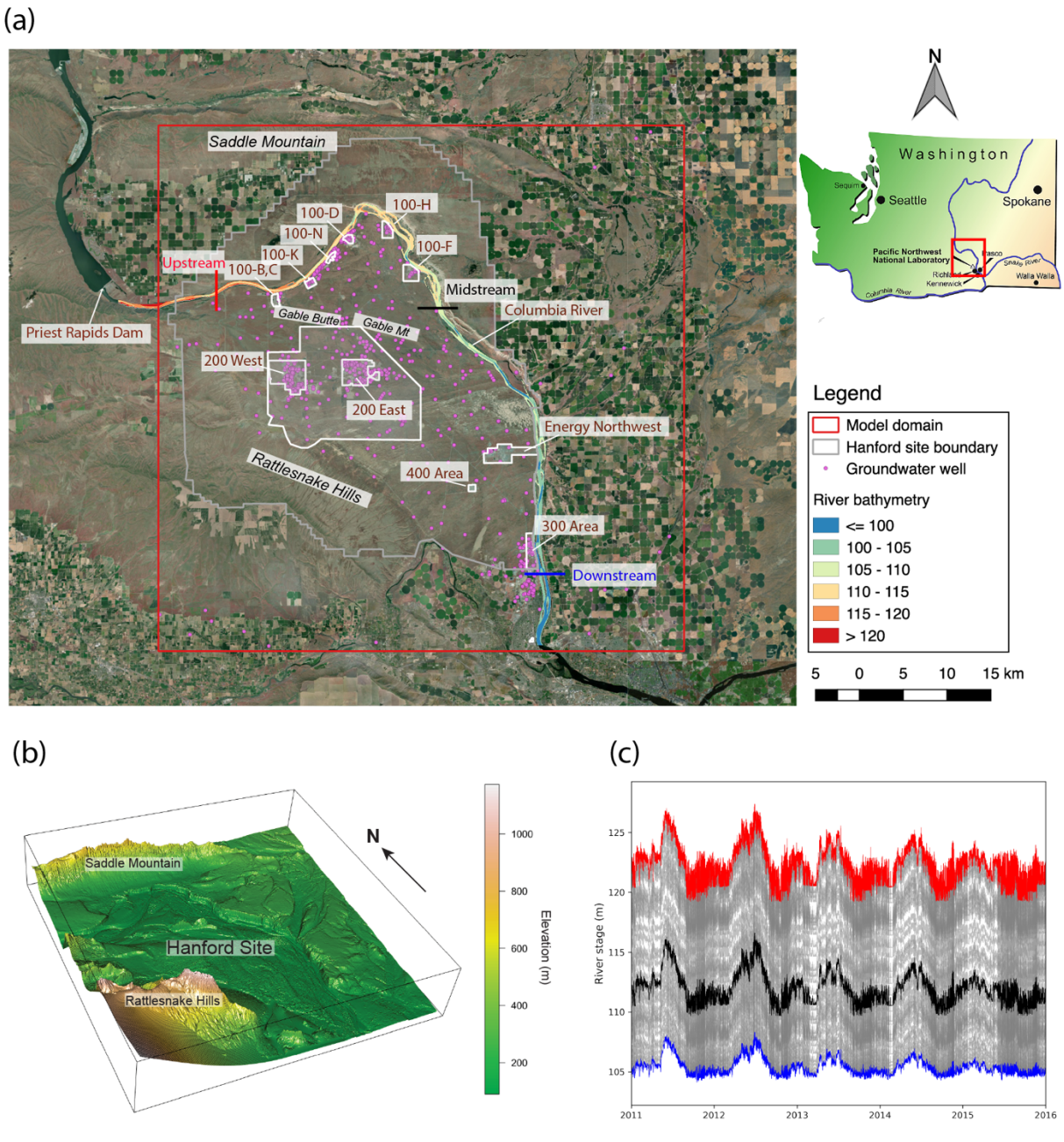

Figure 1. (a) Study site showing the Hanford Reach and Columbia River bathymetry. Hanford Site boundary is outlined with gray line. Former operational areas at the Hanford site are labeled on the map. (b) 3-D representation of land surface topography within the model domain. (c) Hourly river stages along the reach (gray) simulated by MASS1, with highlighted locations at upstream (red), midstream (black) and downstream (blue) as indicated in panel (a).

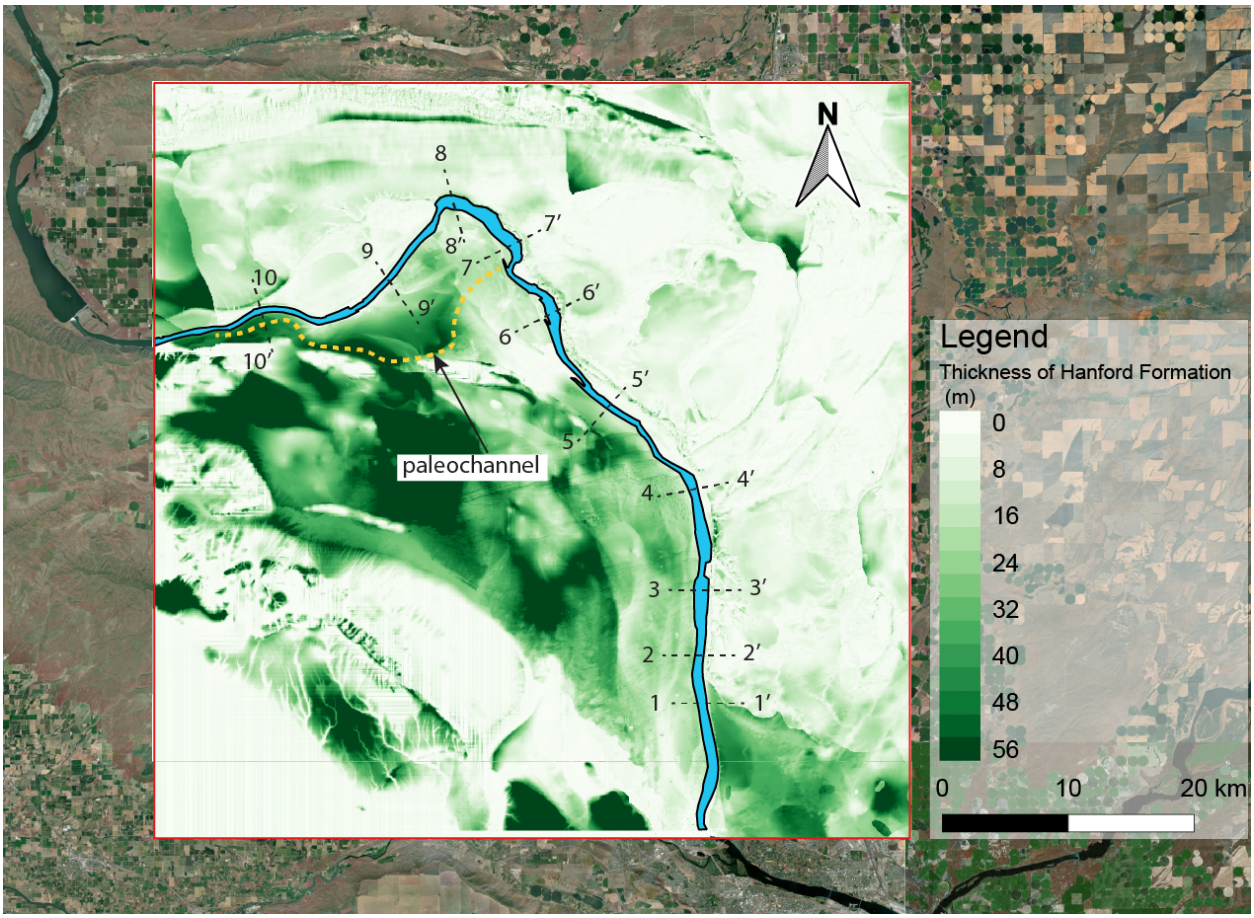

Figure 2. Thickness of Hanford unit within the model domain. The dashed lines (black) are the cross-sectional locations of river segment. Also shown is a paleochannel formed by glacial floods.

Table 1. Hydrogeologic properties of geologic units

Unit	Permeability (m2)	Hydraulic conductivity (m/d)	Porosity	References
Hanford (Hf)	7×10^{-9}	7000	0.2	Williams et al., 2008
Cold Creek (Cc)	1×10^{-10}	100	0.25	Thorne P.D., 2004
Ringold E (Re)	4×10^{-11}	40	0.25	Williams et al., 2008
Ringold Taylor Flats (Rtf)	1×10^{-12}	1	0.43	Drost et al., 1997
Ringold Lower Mud (Rlm)	1×10^{-12}	1	0.43	Drost et al., 1997
Ringold A (Ra)	1×10^{-12}	1	0.43	Williams et al., 2008
Basalt (Ba)	1×10^{-12}	1	0.2	Williams et al., 2008

The Columbia River generally flows from north to south along the Hanford Reach with riverbed elevations ranging from ~125 m upstream to ~90 m downstream Figure 1. River

discharge into the Hanford Reach is regulated by a series of dams including the Grand Coulee Dam and other six run-of-the-river hydroelectric dams. Priest Rapids Dam is the lowest in the series that discharges directly to the Hanford Reach. Load following power generation causes sub-daily to weekly river stage fluctuations of up to 2 m (Arntzen et al., 2006). Additionally, spring snowmelt drives up to 5 m seasonal fluctuations. River discharge ranges from a maximum of ~9880 m^3/s to a minimum of ~1050 m^3/s with an average of ~3390 m^3/s for the last decade. From upstream to downstream, river stage fluctuation is gradually dissipated from ~5 m to ~ 2 m for an average year, with average river stage changing from 122 m to 105 m. Regional groundwater in the unconfined aquifers on both sides of the river is generally flowing towards the river corridor, with an average gradient of 5×10^{-4} m/m and 1×10^{-3} m/m on the west and east side, respectively (Hartman, 2016).

Due to historical nuclear fuels and weapons production, chemical and radioactive wastes were released to the soil surface and vadose zone at the Hanford Site (Hartman, 2016). These releases have created numerous groundwater contamination plumes with concentrations that exceed drinking water standards; some of these plumes discharge directly to the Columbia River. In areas close to the river, contaminant plume behavior is strongly influenced by the river stage fluctuations, creating complex spatial and temporal concentration patterns (Zachara et al., 2016). The Hanford Site maintains a large network of monitoring wells and near-shore aquifer tubes to assess groundwater and river water quality and to trace contaminant plume migration. Geochemical and hydrologic data from these monitoring locations is publicly available (http://phoenix.pnnl.gov).

Significant research has been performed on segments of the Hanford Reach, particularly in the 300 area, to understand groundwater surface water interactions, and its influences on contaminant plume migration, and carbon and nitrogen cycling in the river corridor (Arntzen et al., 2006; Bao et al., 2018; Chen et al., 2012, 2013; Hammond et al., 2011; Hammond & Lichtner, 2010; Johnson et al., 2015; Liu et al., 2015, 2017a, 2017b; Ma et al., 2014; Rockhold, 2013; Stegen et al., 2016; Williams, 2008; Yabusaki et al., 2008; Zachara et al., 2013, 2016; Zhou et al., 2018). Groundwater modeling studies have also been performed for the Columbia River Basin to evaluate regional aquifer resource (Ely et al., 2014; Heywood et al., 2016). Three-dimensional numerical model with a grid resolution of 3 km for the regional Columbia Plateau Regional Aquifer System (CPRAS) encompassing 8.5×10^4 km^2 was constructed to evaluate groundwater availability (Ely et al., 2014). Groundwater pumping was found to have the greatest impact on water levels. In another study, Groundwater model with a grid resolution of 1 km for the East Pasco Basin encompassing 5677 km^2 was developed to simulate groundwater storage change from 1907 to 2013 (Heywood et al., 2016). They found increased groundwater levels in some areas due to increased irrigation. However, these investigations used grid resolution greater than 1 km and focused on deep groundwater flows instead of shallow hyporheic flows.

2.2 Flow and Transport Model

A 3-D groundwater flow and transport model was developed for the Hanford Reach river corridor using PFLOTRAN, a massively parallel subsurface simulator (Hammond et al., 2014). PFLOTRAN solves the Richards' equation (Richards, 1931) for the variable saturated groundwater flow in the porous media, and advection-dispersion equation for conservative solute transport. The model domain (Figure 3) extended 60 × 60 km horizontally and 100 m thick vertically (bottom of the domain is at 50 m above sea level), capturing approximately 75 km of

the river reach from the Priest Rapids Dam to the outskirts of Richland, WA. A uniform structured grid was used with a horizontal resolution at 100 m and a vertical resolution at 2 m. The simulation was run from 2007 to 2015 twice with the first 13 years used as the spin-up to minimize the impacts of the initial condition on the results. The initial and maximum timesteps were 0.01 h and 6 h, respectively.

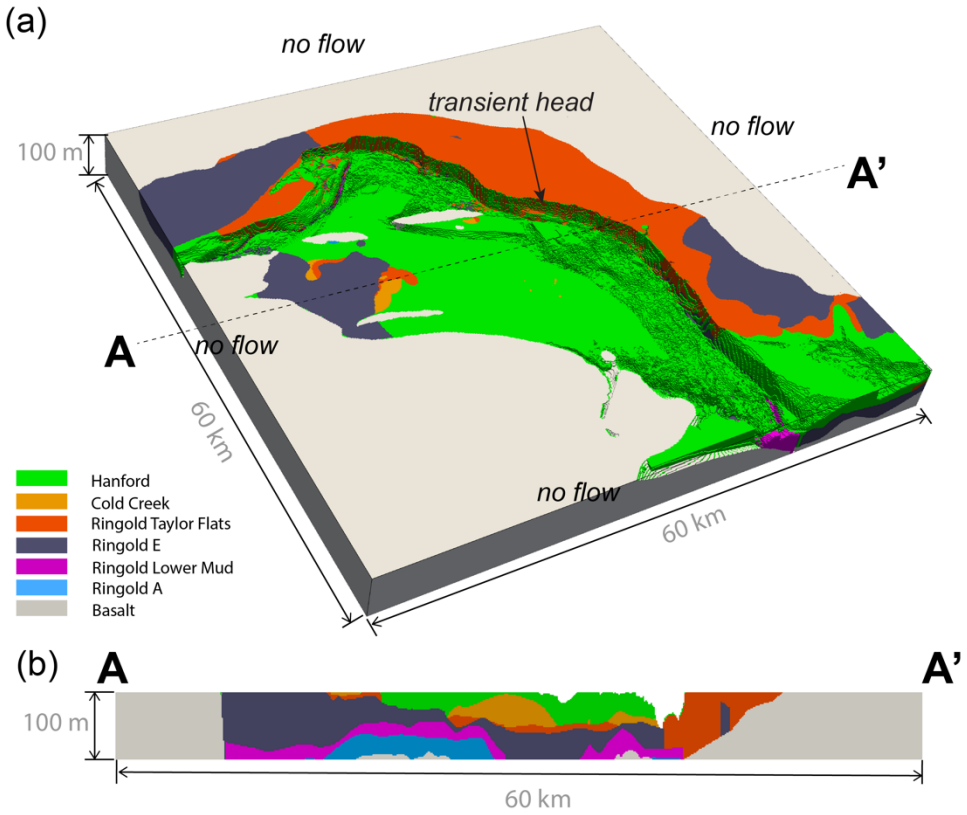

Figure 3. (a) Model domain showing various geologic layers. (b) Cross-section showing model layers

The geologic framework for the study area was developed by merging existing geologic surfaces for the Hanford Site and portions of the Columbia Basin Groundwater Management Area (GWMA) to the east side of the Hanford site. The top surface of the model was constructed by combining land surface topography (Aero-Metric LiDAR 2008, USGS DEM) with Columbia River bathymetry data (Coleman et al., 2010), forming a continuous 30 m grid layer. Geologic layers from the Hanford Site with a grid resolution of 30 m were projected to the North American Vertical Datum of 1988, then mosaicked with common layers with a grid resolution of 30 m from GWMA to form continuous surfaces covering the extent of the study area. Finally, each geologic layer was resampled to match model resolution (100 m). All processing was done using GDAL (GDAL, 2018). Methods used to create surfaces from borehole data and geophysical logs have been described in detail for each respective site (Hammond, 2015). To simplify our model, the permeability field was assumed to be homogeneous horizontally across each geologic unit with the vertical permeability being one tenth of the horizontal permeability.

Hourly river stages during the simulation period were simulated using the Modular Aquatic Simulation System in 1-Dimension (MASS1) (Richmond & Perkins, 2009), calibrated and validated using water surface elevations monitored at several locations along the Hanford Reach with absolute mean errors less than 15 cm (see Niehus et al., 2014 for details). MASS1-simulated river stages from a total of 295 transects perpendicular to the river channel, spacing ~300 m apart, were used as prescribed hydraulic head boundary conditions along the river. The simulated hourly river stages were smoothed using 6-h moving average to facilitate model convergence while preserving sub-daily to daily fluctuations. Pressure head prescribed at each riverbed cell was obtained from linear interpolation using two nearest MASS1 transects. The four lateral boundaries and lower boundary of the model were treated as no flow. The upper boundary was also considered as no flow since the recharge in this area was minimal (~55 cm/yr) (Rockhold et al., 1995). A conductance boundary condition was applied to the riverbed along the reach to emulate the low permeable alluvial layer at the interface between the river and aquifer and to simulate the dampening effects of river pulse propagation into the aquifer (Hammond & Lichtner, 2010). A constant conductance coefficient, the ratio between permeability at river boundary cell and half-cell length, was assumed for the entire river reach. A seepage face was applied at the river-aquifer interface to allow flow into the river. Stress changes below the riverbed associated with river stage fluctuations were ignored since the compressibility of riverbed sediment was rather small.

The initial field of hydraulic head over the model domain was generated using inverse distance weighted interpolation from selected wells where piezometric head measurements were available at the starting time. A conservative tracer with a concentration of one representing 100% river water was released along the river shoreline to track the movement of river water into the subsurface. Groundwater was initially assigned a tracer concentration of zero everywhere (i.e. 0% river water). Riverbed transport boundary conditions were employed such that river water tracer flowing into groundwater aquifer is assigned a specified concentration (Dirichlet) while river tracer flowing out has a zero diffusive gradient (zero-gradient) (Lichtner et al., 2015). The top, bottom and four lateral boundaries were treated as no flux boundaries for the river tracer.

3. Results and Discussion

To examine the sensitivity of simulated HEFs as well as the flow and transport processes to model grid resolutions, various grid resolutions were tested under the same boundary and river flow conditions. Hydrologic exchange flux was more sensitive to vertical model resolution than horizontal model resolution under the same model setup. Using the same horizontal resolution of 100 m, a model with a vertical grid resolution of 2 m induced ~20% more exchange volume than a vertical grid resolution of 5 m. Using the same vertical resolution of 2 m, a model with a horizontal resolution of 100 m induced ~7% more exchange volume than a horizontal resolution of 200 m. These results indicated that refining vertical model resolution could be more important than refining the horizontal one for accurately quantifying the exchange flux across river-aquifer interface. Although we could refine the model resolution further both horizontally and vertically, the growing problem size combined with scalability limit of the PFLOTRAN simulator made the computational cost unmanageable beyond the horizontal resolution of 100 m and vertical resolution of 2 m. Therefore, all the results reported here were based on the 100 m × 100 m × 2 m resolution.

3.1 Groundwater Flow and River Tracer Dynamics

Groundwater elevation contours simulated by PFLOTRAN showed that the regional groundwater was generally flowing towards the river with a larger gradient on the east side as compared to the west side (Figure 4 (b)). The flow directions in the near shore area changes frequently with the fluctuation of river stages. River water intrusion into the groundwater aquifer occurred when river stage was rising while groundwater discharge into the river in response to falling stages. The extent of hydraulic pressure front propagation varied along the reach and over time as illustrated in the animation provided in the supplementary information (Movie S1).

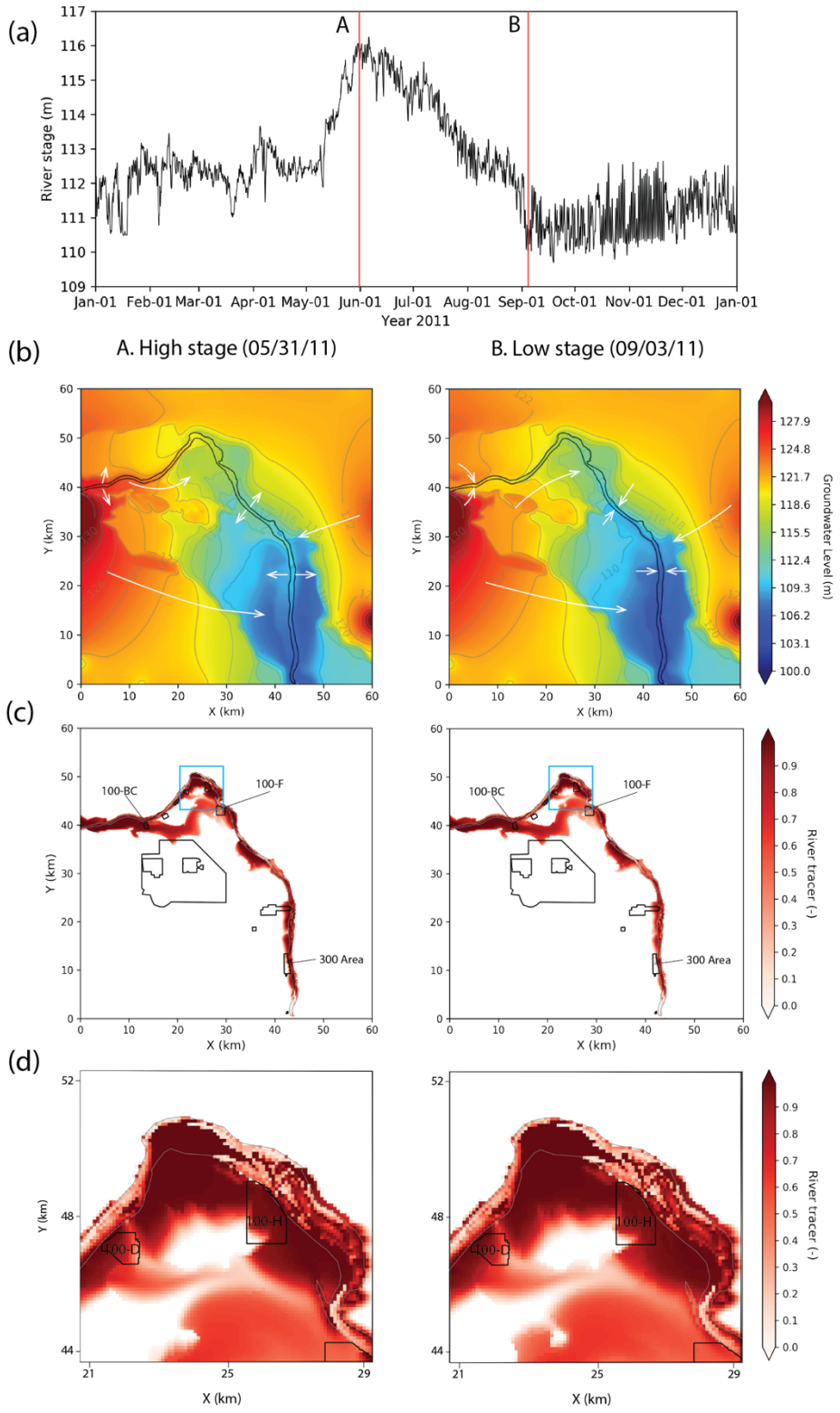

292

293 Figure 4. (a) River stages during year 2011 at midstream location; (b) groundwater table contour at high and low
294 river stages, with white arrows indicating the flow directions; (c) river tracer plume along the reach at high and low
295 river stages; and (d) Enlarged river tracer plume near the horn area.

296 The conservative river tracer plume expanded and contracted as river stage rose and fell
297 along the river channel as can be observed from the animation in the supplementary information
298 with two example snapshots shown in Figure 4 (c)(d). River water intrusion extent varied along
299 the river corridor from upstream to downstream depending on the local geomorphology, similar
300 to the propagation of hydraulic pressure wave front. The greatest intrusion occurred at an
301 upstream location (near 100-BC Area) where river water was following a preferential flow path
302 shaped by the paleochannel that was filled with coarse Hanford sediment (Figure 2), and
303 discharged towards the 100-F Area (Figure 4(d)). For the downstream segment of the reach (near
304 300 Area), river water only intruded as far as ~1 km laterally.

305 **3.2 Hydrogeomorphic Controls on Hot Spots and Hot Moments of HEFs**

306 The Darcy flux across river cell faces was output from PFLOTRAN to assess the
307 magnitudes and directions of HEFs. A positive flux was defined as groundwater discharging to
308 the river from the aquifer (i.e., river gaining) while a negative flux was river water intruding to
309 the groundwater aquifer (i.e., river losing). Hydrologic exchange flux across the riverbed showed
310 strong spatial and temporal variability across the reach as shown in Figure 5. The effects of river
311 stage fluctuations, channel morphology and subsurface hydrogeology on HEFs are examined
312 below.

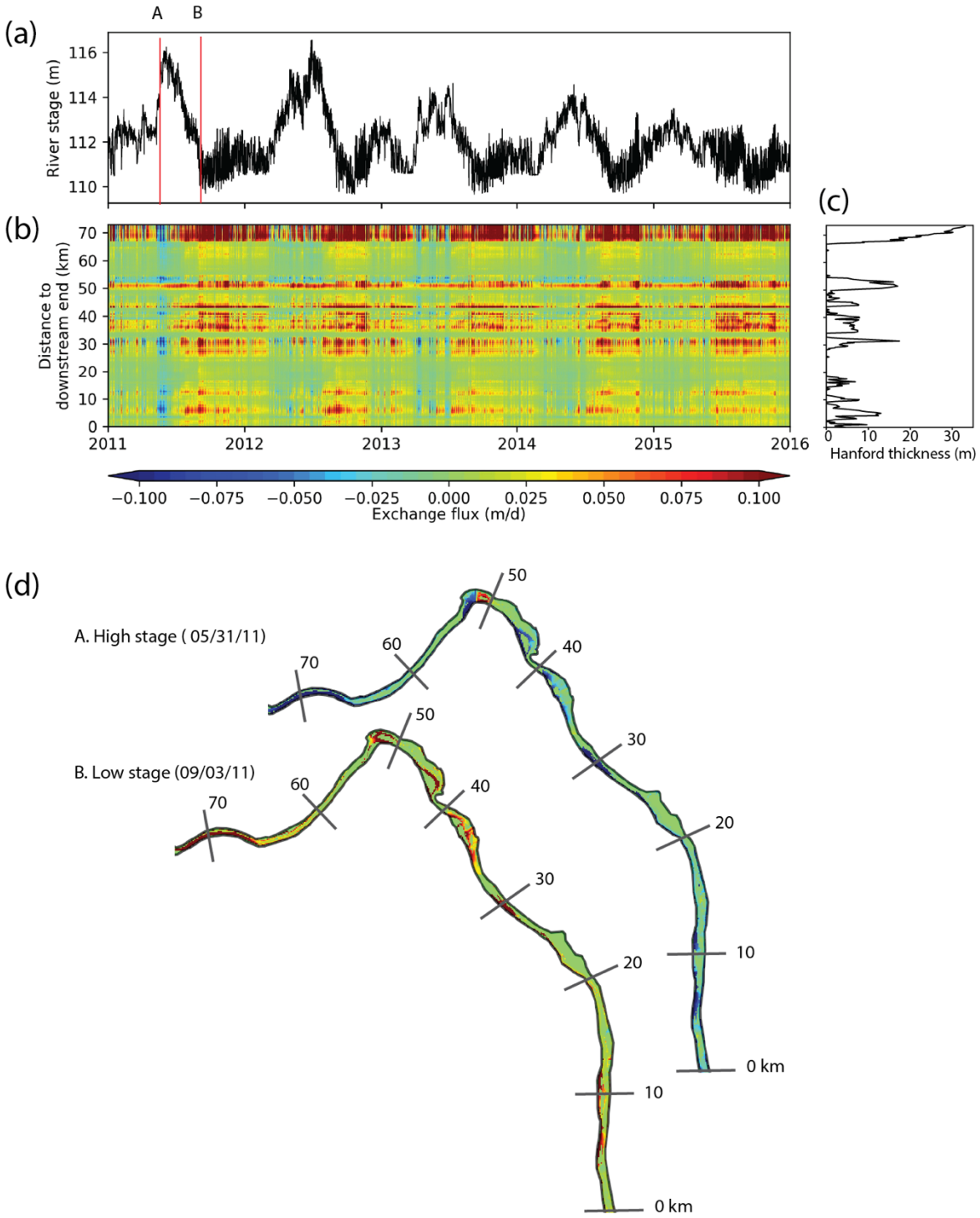

Figure 5. (a) River stages at midstream location (~ 40 km from downstream end) during simulation period from 2011 to 2015. (b) Heat map showing the spatial (vertical axis, where 0=downstream end of the Hanford Reach and 75=tailrace of Priest Rapids Dam) and temporal (horizontal axis) patterns of HEFs. (c) Average Hanford Formation thickness across the river reach. (d) Two snapshots of HEFs across the riverbed at high and low river stages.

3.2.1 The Effects of River Stage Fluctuations

It can be observed from Figure 5 (a)(b) that the hot moments of HEFs (times of high exchange flux rates) coincided with times when river stage experienced sharp changes, both in the rising and falling regimes. When the river stage was rising in response to spring snowmelt in the watershed headwaters, river was in general losing water to the adjacent groundwater aquifer (i.e., negative HEFs) despite some gaining spots due to local hydrogeologic or hydromorphic heterogeneity (Figure 5(d)). River turned to gaining water from the groundwater aquifer (i.e., positive HEFs) when the river stage started to fall after the peak flow in early summer. Two snapshots of HEFs across the riverbed at high and low river stages in year 2011 (Figure 5(d)) revealed the spatial distribution of HEFs. During high river stage (05/31/2011), HEFs were mostly negative except at the segment between 50 and 52 km from the downstream end. The positive flux was resulted from the strong lateral cross-meander flow in the horn area. During low river stage (09/03/2011), flux rates were dominantly positive across the reach indicating strong groundwater discharge. Average flux rates were -0.04 m/d and 0.05 m/d for the high and low river stages, respectively. The most significant period of losing river flow condition occurred between 05/10 and 05/30 of 2011 when the river stage rose almost 4 m. Strong gaining river flow condition occurred at base flow when river stage was low. Our results showed that dynamic river fluctuations induced frequent flow reversals across the riverbed, which otherwise would be minimal under steady flow conditions.

3.2.2 The Effects of Channel Morphology and Subsurface Hydrogeology

Hot spots (areas with higher exchange flux relative to the surroundings) of HEFs could be identified from the heat map in Figure 5(b), where high HEFs occurred consistently over the season and years. River channel morphology including sinuosity is known to play an important role in driving lateral hydrologic exchange flows in the riparian zone (Cardenas, 2009), whereas subsurface hydrogeology including sediment permeability and thickness controlled the extent of vertical exchange. The hot spots of HEFs coincided with the peak of Hanford thickness (Figure 5 (c)). Furthermore, the Hanford Reach was divided into 10 segments (shown in Figure 6 (a)) based on the locations of hot spots to examine the individual effects of channel sinuosity and permeable sediment thickness on exchange flux. Sinuosity and the average thickness of permeable sediment (i.e. Hanford unit) were calculated for each river segment. The cumulative exchange flux per channel length was calculated for each segment over the simulation period between year 2011 and year 2015. As shown in Figures 6(b-c), river segment #10 in the upstream end had a relatively small sinuosity (1.07) but the largest exchange flux per channel length (1.26×10^7 m^3/km) because of the thick Hanford sediment (~ 12 m). In comparison, river segment #8, located along the horn area, had the largest sinuosity (1.3) but the second largest exchange flux per channel length (~ 9.28×10^6 m^3/km) because of a thinner layer of Hanford sediment (~ 6 m). Likewise, river segments #9 and #4 had a sinuosity of ~1.05 and the smallest exchange flux per channel length due to a thin presence of Hanford unit. For river segments with similar sediment thickness (i.e. #1 and #7), segment #7 with larger channel sinuosity induced larger exchange flux compared to segment #1.

Linear regression was performed on the exchange flux per channel length against sinuosity and thickness of Hanford unit. In general, exchange flux per channel length increased with channel sinuosity and thickness of Hanford unit (Figure 6(b&c)). Thickness of Hanford unit had a stronger positive correlation with the exchange flux with an r-square of 0.95 compared

to 0.47 with the channel sinuosity. Analysis of variance (ANOVA) performed on the exchange flux per channel length against the channel sinuosity and Hanford thickness (Table 2) showed that Hanford thickness had a p-value close to zero as compared to 0.13 for sinuosity, indicating that Hanford thickness was statistically significant while sinuosity was not. Hanford thickness explained 87.3% of the total variance in exchange flux, while sinuosity only explained 3.7%. Overall, the exchange flux per unit channel length was dominated by the thickness of the Hanford Formation sediment, with channel sinuosity playing a secondary role.

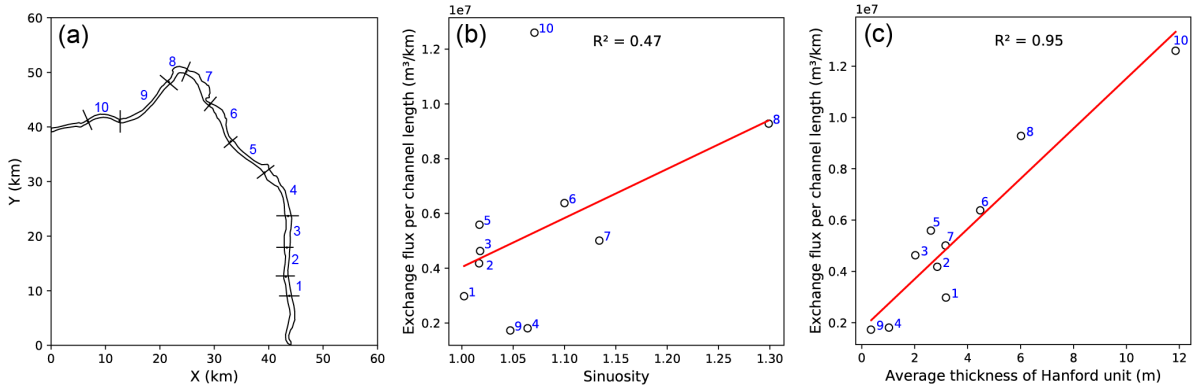

Figure 6. (a) Numbered river segments along the Hanford Reach. (b) Relationship between exchange flux per river channel length and river channel sinuosity. (c) Relationship between exchange flux per river channel length and the average thickness of Hanford Formation sediment below the riverbed. Also shown are the linear regression lines (red) and R-squared values.

Table 2. ANOVA summary table for exchange flux against sinuosity and thickness of Hanford Formation

Source of variation	Sum of squares	Degrees of freedom	F ratio	p-value	Variance explained (%)
sinuosity	3.08×10^{12}	1	2.89	0.13	3.70
thickness	7.23×10^{13}	1	68.06	7.50×10^{-5}	87.30
residual	7.44×10^{12}	7	NaN	NaN	NaN

A cross-sectional plot of the river tracer plume corresponding to time of the high river stage (05/31/11) along with hydrogeologic units was provided at each river segment in Figure 8 to further investigate the effect of subsurface hydrogeology such as underlying low- or high-permeability geologic layers on HEFs. The consolidated Ringold Formation or basalt acted as aquitards due to their low permeability compared to the Hanford Formation. The movement of river tracer was found to be inside the Hanford unit following the topography of the underlying aquitard. Significant river water intrusion occurred in areas with thick underlying Hanford sediments. For example, slices 5-5', 7-7', 8-8' and 10-10' showed large lateral intrusion of river tracer with a distance as far as 2.5 km. Among those, slice 10-10' displayed the largest vertical intrusion of 25 m because of the presence of thick Hanford Formation. On the contrary, minimal river water intrusion occurred when the channel was surrounded by less permeable Ringold sediments or basalt. For example, slices 1-1', 2-2', 3-3', 4-4', 6-6' and 9-9' showed less river tracer intrusion with an average lateral distance of 1 km. Therefore, subsurface topography,

particularly the local elevation of aquitards, controlled river water intrusion extent and modulated the magnitude of HEFs between river and aquifer. Similarly, the topography of bedrock has been shown to control the dynamic patterns of subsurface storm flow at the hillslope scale elsewhere (Freer et al., 2002).

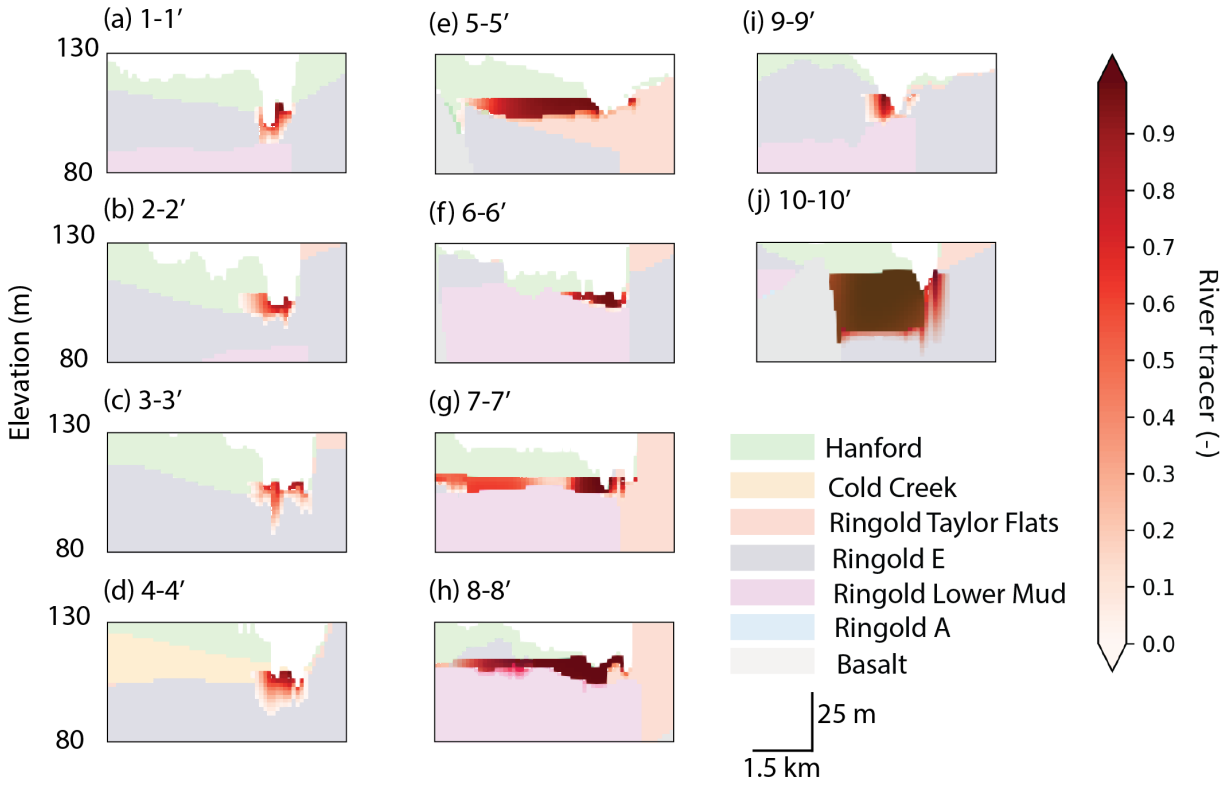

Figure 7. (a-j) 2-D cross-sections showing the extent of river tracer plume overlying geologic units. Note that geologic unit color scheme is the same with Figure 3 but with 80% transparency to allow the demonstration of tracer plumes.

3.3 The Impacts of High-Frequency Flow Variations Induced by Dam Operations

A weekly moving average was applied to the hourly river stages as a low-pass filter to remove sub-daily, daily and weekly frequency to mimic the scenario without high-frequency dam operations (i.e. weekly smoothed case), which are often referred to as hydropeaking. Spectral analysis using Fast Fourier Transform (FFT) (Bloomfield, 2000) showed that river stage under weekly smoothed case was filtered out of sub-daily, daily and weekly fluctuation signals as compared to the base case (Figure 8 (b)). Similarly, spectral analysis of exchange flux at the midstream location showed that daily frequency was dominant under the base case while most high-frequency signals were absent for the weekly smoothed case (Figure 8 (d)).

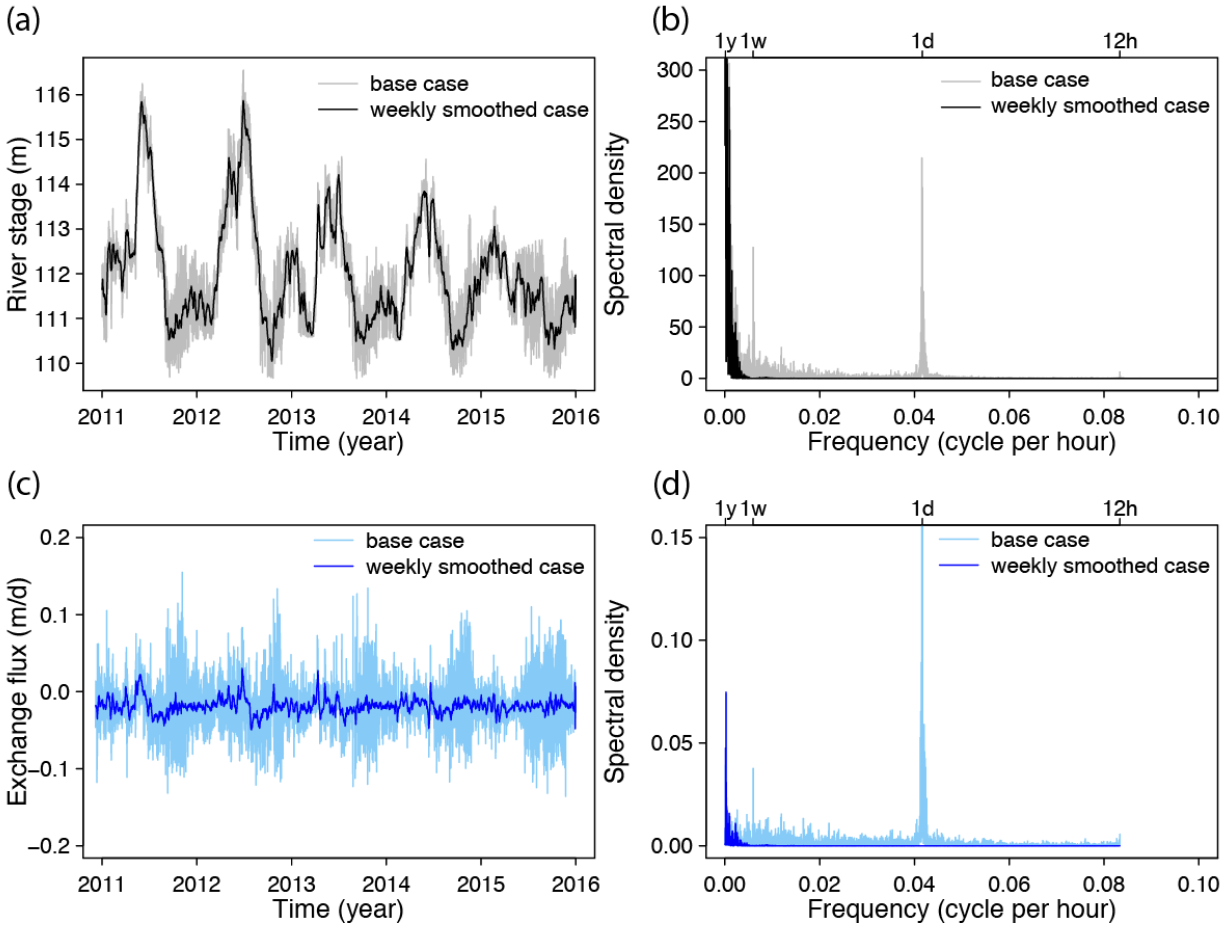

Figure 8. Spectral analysis for two river boundary conditions at midstream location using FFT. (a) River stage time series under both cases. (b) Spectral analysis for river stage under both cases. (c) Exchange flux time series under both cases. (d) Spectral analysis for exchange flux under both cases.

3.3.1 Comparison of spatiotemporal patterns in exchange flux

The spatial and temporal pattern of exchange flux across the riverbed was similar under both cases (Figure 9). However, the weekly smoothed case induced smaller overall exchange flux rates (both gaining and losing) and less frequent fluctuations between gaining and losing conditions. Histograms revealed that the distribution of exchange rates under the base case had similar shape but a broader distribution than the weekly smoothed case (Figure 10 (b)). The majority of the flux rates were centered around 0 m/d indicating that the river was neither gaining or losing. The maximum and minimum flux rates for the base case were 0.493 m/d and -0.617 m/d, as compared to 0.213 m/d and -0.245 m/d for the weekly smoothed case. A one-to-one scatter plot displayed strong correlation between flux under both cases (Figure 10 (c)). High-frequency flow variations greatly enhanced the magnitudes of exchange flux. High-frequency flow variations led to either (1) enhanced exchange flux with no changes in flow direction (gray, 76%); (2) changes in flow direction from losing to gaining (red, 9%); and (3) changes in flow direction from gaining to losing (blue, 15%). In total, high-frequency flow variations accounted for 24% of the flow reversals.

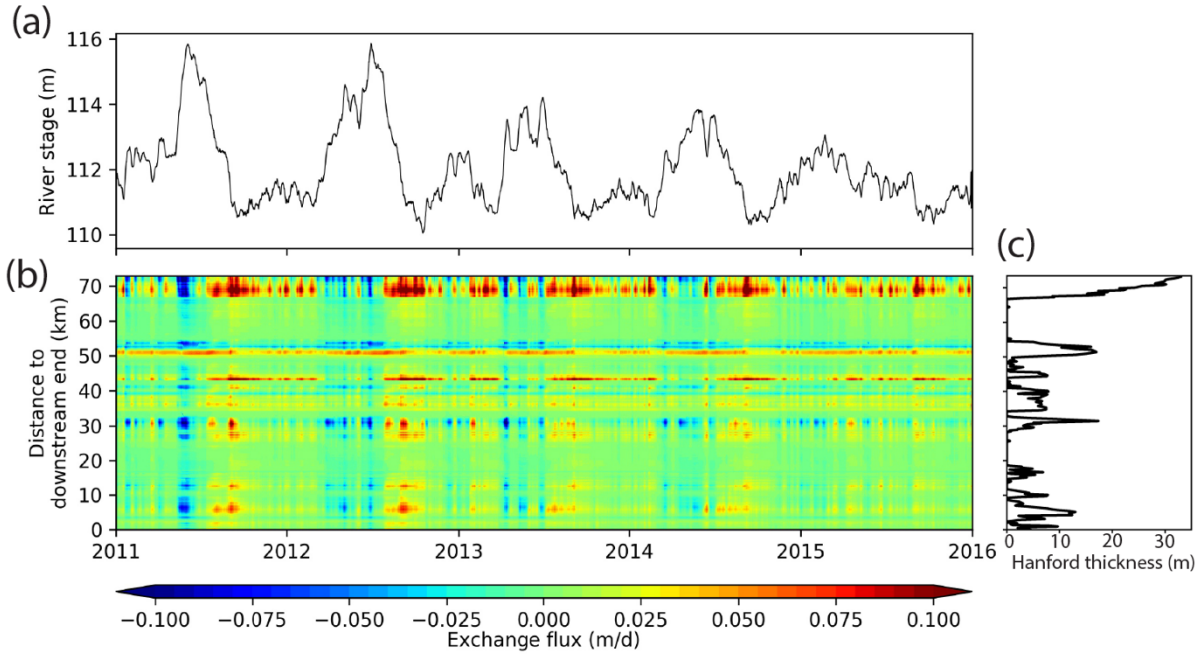

Figure 9. (a) River stage for weekly smoothed case at midstream location. (b) Heat map showing temporal-spatial distribution of exchange flux across the riverbed. (c) Average thickness of Hanford Formation across the river reach.

In general, river switched from gaining to losing under the base case when river stage was low (blue flux in Figure 10(d)). River switched from losing to gaining under the base case during times when river stage was high (red flux in Figure 10(d)). In other words, high-frequency stage fluctuations induced by dam operations could reverse a normally gaining river under low flow condition to a losing river, and a normally losing river under high flow condition to a gaining river.

Our results demonstrated the importance of high-frequency flow variations in driving high frequent exchange between river and aquifers, therefore increased the potential for biogeochemical reactions. The effects of high-frequency flow variations on thermal regimes and biogeochemical reactions in hyporheic zone was more pronounced when river stage was low during fall and winter (Song et al., 2018). In an earlier study, high-frequency flow variations were attributed to the maximum accumulation of U(VI) fluxes to the Columbia River at the Hanford 300 Area (Hammond & Lichtner, 2010).

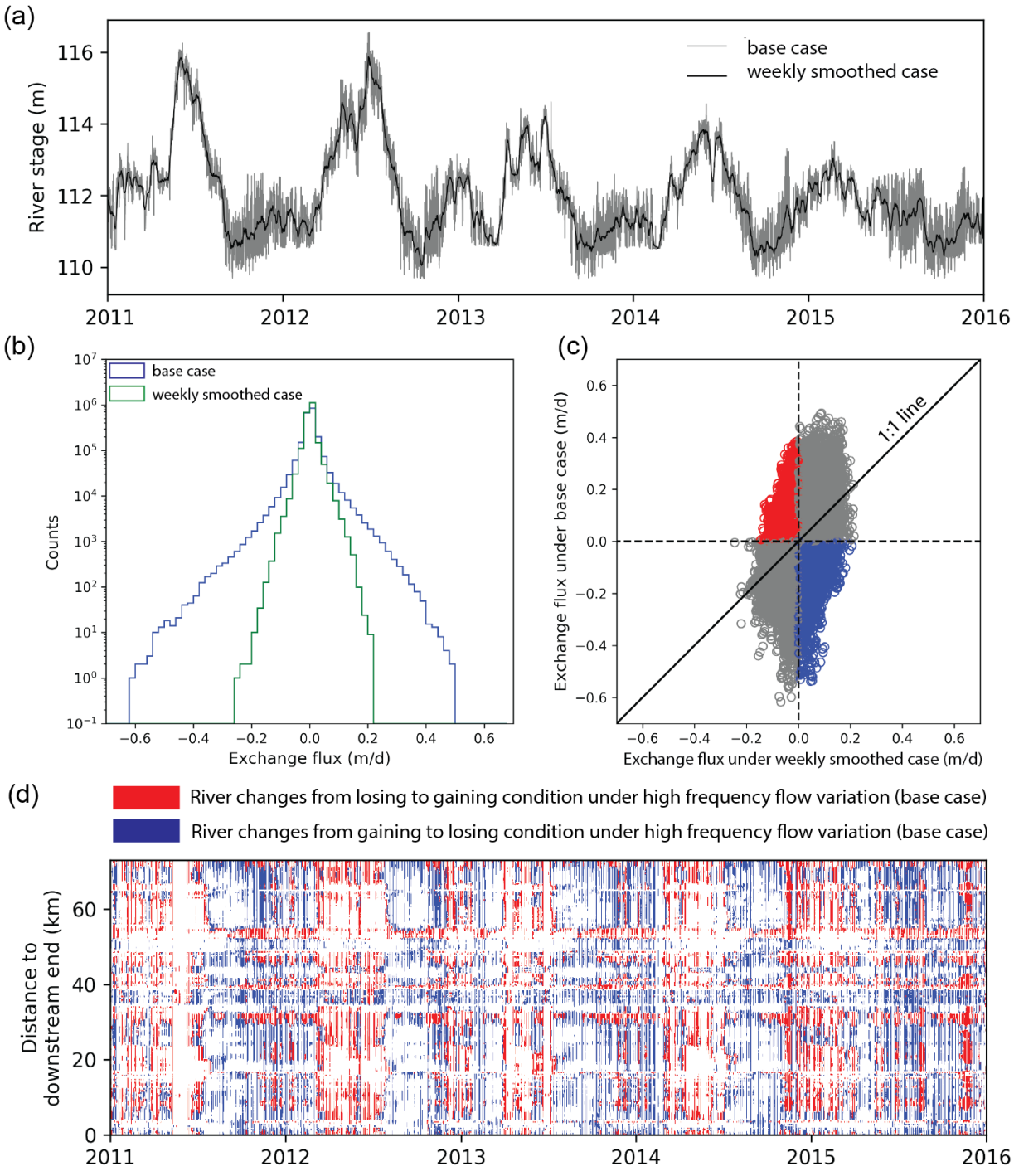

Figure 10. (a) River stage over the simulation period under both cases. (b) Histograms of HEFs in both cases. (c) Scatter plot between flux rates under both cases. Red and blue circles correspond to the red and blue fluxes in panel (d). Also shown is the one-to-one line (black). (d) Heat map showing changes in HEF directions. River switched from gaining to losing (blue) and from losing to gaining (red).

3.3.2 Comparison of interannual variability in exchange volume

Aggregated gaining, losing, net, and total exchange volumes were calculated over the entire Hanford Reach on annual basis using the Darcy flux across the aquifer-river interface:

$$V_{gain} = \int_0^T \int_\Omega Q_i(t) dS_i dt \ , \ when \ Q_i(t) \geq 0 \quad (1)$$

$$V_{lose} = -\int_0^T \int_\Omega Q_i(t) dS_i dt \ , \ when \ Q_i(t) < 0 \quad (2)$$

$$V_{net} = \int_0^T \int_\Omega Q_i(t) dS_i dt \quad (3)$$

$$V_{total} = V_{gain} + V_{lose} \quad (4)$$

where $Q_i(t)$ is Darcy flux for cell face i at time t, S_i is the area for cell face i, Ω is the total river channel area, and T is the time window of the aggregation (i.e., one year). V_{gain}, V_{lose}, V_{net} and V_{total} are the gaining, losing, net and total exchange volumes per year, respectively.

The exchange volumes for the weekly smoothed case displayed similar interannual variability to that under the base case (Figure 11). Wet years (e.g.,2011 and 2012) exhibited larger V_{total} compared to that under a dry year (2015). Similarly, V_{gain} and V_{lose} were higher in wet years than those in average and dry years. In general, river was losing during wet years while river was gaining during dry years. Gaining river conditions followed wet years when water stored in the aquifer flowed back to the river. Compared to the upstream dam discharge, only a small fraction (~0.5%) of the total river volume was exchanged with groundwater in passage through the reach on an annual basis.

On average, the high-frequency flow variations induced 76% more V_{total} compared to the weekly smoothed case. Average V_{gain} and V_{lose} were smaller for the weekly smoothed case. However, the annual net exchange volumes (V_{net}) were comparable under both cases.

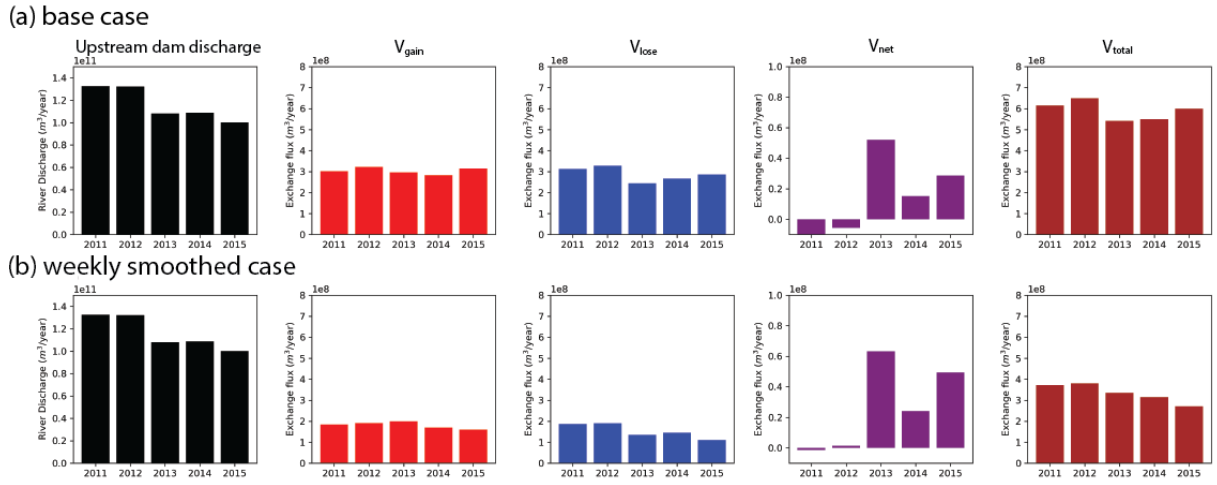

Figure 11. Annual river gaining, losing, net and total exchange volume under both cases. Note the scale difference for V_{net}.

3.4 Implications of HEFs on Contaminant Plume Migration

Hydrologic exchange flows under high-frequency flow variations have important implications for contaminant plume monitoring and remediation within the river corridors that experience regular, periodic river water intrusions. River intrusions during high river stages may dilute a contaminant plume or portions of it, and carry contaminants in various directions. During low river stage, groundwater could carry the contaminants back towards the river in different trajectories. High-frequency flow variations greatly enhanced the amount of water exchanged across the river-aquifer interface, leading to an increase in the contact time between river water and biogeochemically reactive subsurface sediment. Increased contact time had great potential for biogeochemical transformation and immobilization of contaminant in the subsurface.

The river water influence area as indicated by the conservative river tracer plume and historic river corridor contaminant plumes (2010) showed strong similarities in their migration paths (Figure 12). For example, extensive plumes of Cr, a primary contaminant resulting from routine disposal of reactor coolant which contained a corrosion inhibitor of sodium dichromate, were found near the 100-D and 100-H areas migrating across the horn area (Hartman, 2016). The intrusion of Cr-free river water from the 100-D area would dilute and disperse the Cr plume along the flow path, which eventually is discharged back to the river at the 100-H area (Figure 12 (b)). River intrusion would also bring in more dissolved oxygen and dissolved organic carbon which enhances microbial activities in the subsurface and mobilizes Cr (Yang et al., 2018). Another source of Cr was identified at the 100-BC area (Hartman, 2016) along the preferential flow path of river water intrusion. It is highly possible that the Cr plume found near the 100F area was migrated from the 100-BC area with the preferential flow.

For contaminant sources near 100-K and 100-N areas, the impact of river intrusion was limited by a low permeable layer in the subsurface which formed a barrier for river inflows. Similar to chromium, a tritium plume showed similar source locations and possible migration paths in response to river intrusion (Hartman, 2016). For nitrate, a large contaminant source was identified at the 100-F area and was moving southward with the hyporheic corridor flow. These comparisons clearly indicated that contaminant plume migration in the river corridor was strongly influenced by groundwater-surface water interactions. Special attention should be paid to contaminant sources that lie along the preferential flow paths created by subsurface structures and heterogeneous properties.

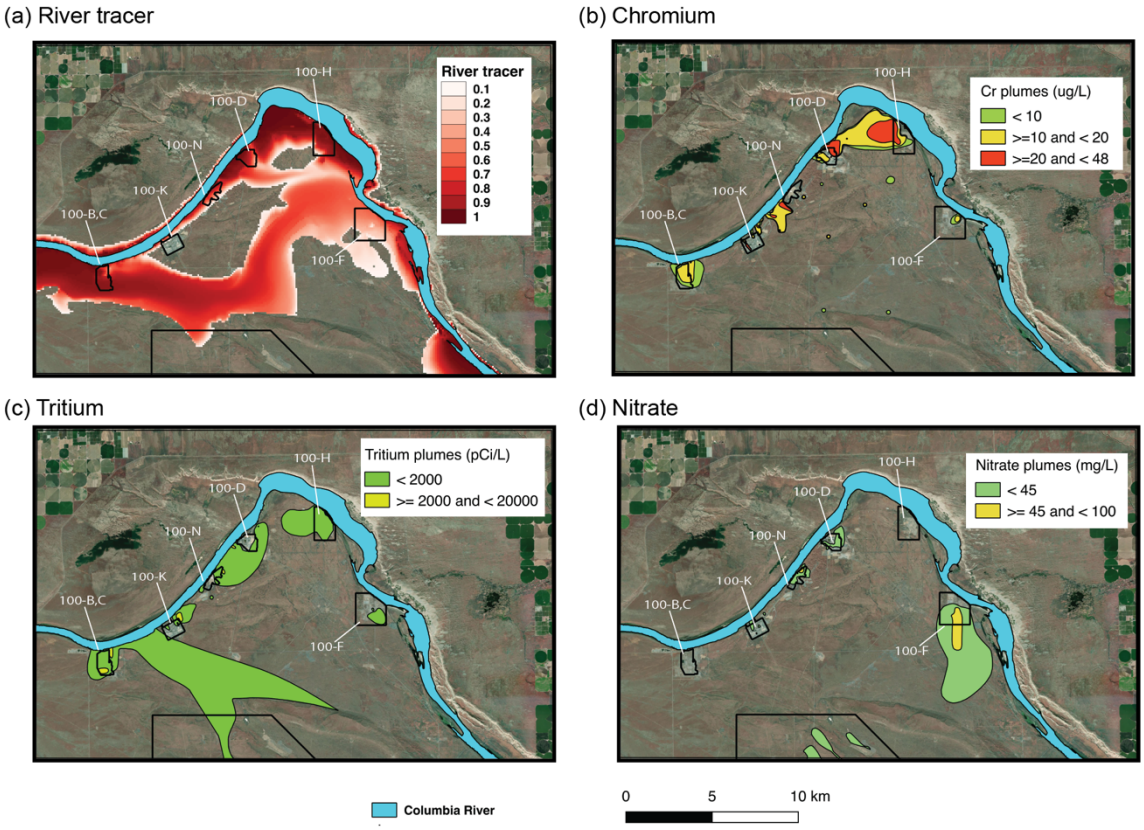

Figure 12. (a) Simulated river tracer plume (b) Chromium plumes (c) Tritium plume and (d) Nitrate plume at Hanford horn areas in year 2010.

3.5 Challenges and Limitations of Current Work

To our knowledge, this study is the first one to mechanistically simulate reach-scale hydrologic exchange as influenced by dynamic river stage variations, channel morphology, and subsurface hydrogeology at a relatively fine resolution. However, the limited field data, complex geologic settings, and parameter uncertainties pose great challenges in developing the model and producing realistic results, along with the growing computational expense with the need to refine model resolutions.

Despite the large number of groundwater wells existing within the model domain, many wells did not have continuous measurement of groundwater elevation, especially on the east side of the river and near the model boundaries. Therefore, we could not implement prescribed head boundary conditions along the model boundaries as we did in smaller models (Zachara et al., 2016). Instead, no-flow boundary conditions were applied to the lateral model boundaries, which was justified by the observed exposure of impermeable basalt along a significant portion of the model boundaries.

Our model did not fully capture the complex geologic units with varying topography and heterogeneous permeability at the field site. The permeability of each geologic unit was assumed

to be homogeneous with oversimplifying vertical anisotropy. The permeability values were originated from a few local field experiments (within ~1 km^2 footprints). Thus, they may not represent the full range of variability in the formations at the entire reach scale. Moreover, riverbed conductance, an coefficient associated with the permeability and thickness of alluvium layer at river bottom, was assumed to be constant across the entire reach, although it was shown to be the most sensitive parameter in calculating exchange flux across river-aquifer interface (Bao et al., 2018; Hammond & Lichtner, 2010). Spatially distributed conductance values, if mapped in future characterization efforts, could likely change the spatiotemporal patterns of the HEFs. In addition, fine-scale morphologic features with size smaller than a grid cell (100 m), such as in-channel bedforms (i.e. bars, dunes, pool-step or pool-riffle sequences),were not resolved in the current model, even though they are important in driving short flow paths across the riverbed (Magliozzi et al., 2018). Those local exchanges are likely contributing a small portion to the total HEFs at the larger spatial scale of a river reach (Boano et al., 2014).

Simulated groundwater levels and tracer breakthrough curves at selected wells with known screen intervals were compared with observed water table and specific conductance measurements (see supplemental information Figure S3-S5) to provide a preliminary assessment of our numerical model in representing the real system. Overall speaking, simulated water table elevations in the near-shore wells (within 250 m from the shore) showed reasonable match to the observations with a root-mean-squared-error (RMSE) smaller than 0.5 m. Mismatches greater than 1 m were yielded in some more inland wells (> 250 m). Simulated river tracer concentrations were in qualitative agreement with the observed specific conductivity (SpC) at the near-shore wells — a spike in river tracer concentration roughly corresponded to a dip in SpC, both indicating arrival of river water in the groundwater aquifer. A full suite of sensitivity analysis could be performed to identify pathways to improve the numerical model for the site, through assimilating existing observations or additional data collection, which is beyond the scope of the current study.

3.6 Implications to Other River Corridor System

It should be noted that our site has the following unique features that may not exist in other river corridor systems: (1) The Hanford sediment forming the top unconfined aquifer is highly permeable (~7000 m/d), which allows the river water to penetrate several kms inland; (2) The high discharge volume as well as high magnitude of variations in its sub-daily, daily as well as seasonal discharge and river stage associated with such a high-order regulated river; (3) long-term, spatially extensive hydrologic, geologic and geochemical datasets are available resulted from the Hanford remediation efforts. Nonetheless, numerical modeling is a general approach that can be applied to other river corridor systems.

Our findings of high-frequency dam operations enhanced hydrologic exchange are consistent with other river systems that experience regular, periodic fluctuations. For example, Sawyer et al. (2009) found that frequent river fluctuations increased the extent of hyporheic zone which otherwise would be limited under base flow condition in Lower Colorado River (Texas, USA) with dam-induced daily river stage fluctuations close to a meter. In a small incised coastal river (Delaware, USA) that experiences semi-diurnal tidal fluctuation of 0.75 m, at least 11% river water was found to exchange through tidal bank storage (Musial et al., 2016), while the tides drove dissolved oxygen to penetrate further and deeper into the bank compared to similar non-tidal rivers. Such alterations in HEFs could fundamentally change the transport of riverine

nitrate and dissolved organic carbon into the aquifer, consequently impact the microbial activities and biogeochemical reactions in the river corridor, such as the denitrification hot spots in the regulated system studied by Shuai et al. (2017) under gaining river condition.

Our study showed that high-frequency river stage fluctuations induced frequent flow reversals across the river-aquifer interface. The total exchange volumes could be significantly underestimated without accounting for those high-frequency variations, which has to be supported by high-resolution field data and high-resolution numerical models. We showed that the thickness of permeable geologic unit or the depth to confining layer played an important role in controlling the hot spots of exchange flux and the extent of river water intrusion, implying that hydrogeology of the river corridor systems should be characterized and incorporated into the model to better understand HEFs in other systems.

4. Conclusions

We developed a 3-D, coupled, variably saturated flow and transport model to investigate the hydrogeomorphic factors that control the locations and magnitude of hydrologic exchange flows under dynamic river fluctuations for the Hanford Reach. Specifically, we looked at the effects of river stage fluctuations, channel morphology and subsurface hydrogeology on hot spots and hot moments of hydrologic exchange flows. Our results showed that HEFs exhibited strong spatial and temporal patterns across the entire reach during the simulation period as well as interannual variabilities. Wet years yielded larger total exchange volumes than those under dry years. In general, the Columbia River was gaining all year around, except during large rise in river stage during late spring and early summer.

Hot moments of hydrologic exchange were controlled by the timing and magnitude of river stage fluctuations. Large hydrologic exchange flux rates were linked to dramatic changes in river stage magnitude. Hot spots of hydrologic exchange were controlled by both river channel morphology (sinuosity) and subsurface hydrogeology (the thickness of permeable Hanford unit). In general, exchange flux per channel length increased with channel sinuosity or the thickness of permeable sediment. However, permeable sediment thickness played a dominant role in controlling the exchange flux. Subsurface topography, particularly the local elevation of aquitards, controlled river water intrusion extent and modulated the magnitude of flow exchange between the river and the aquifer. The topography of underlying impermeable units created preferential flow paths where deep paleo-erosional features were present. When developing conceptual models at the river reach and watershed scales, topography of the relatively impermeable geologic unit should be characterized and represented in the model to better understand the HEFs in river corridor systems.

High-frequency flow variations induced by dam operation drove high frequent flow reversals across river-aquifer interface, and resulted in ~ 76% more total exchange volume than that under the weekly smoothed case. In addition, high-frequency flow variations induced 24% more flow reversals than the weekly smoothed case. Frequent flow reversals as a result of dam operation could increase the potential for biogeochemical reactions. Compared to historic contaminant plumes at Hanford Site, our heuristic conservative tracer plumes revealed the potential influence of river water intrusion on the migration of contaminant plumes, particularly for contaminant sources located within the preferential flow path shaped by deep paleochannels. Our modeling approach and main findings are transferrable to other river corridor system that experience regular, periodic fluctuations. Priority should be given to collect high resolution time

610 series data for river stage, and apply that to the river boundary. The surface of less permeable
611 geologic layer or aquitard should be incorporated into the model if it is within domain of interest.
612
613
614

Acknowledgments

This research was supported by the U.S. Department of Energy (DOE), Office of Biological and Environmental Research (BER), as part of BER's Subsurface Biogeochemical Research Program (SBR). This research used resources of the National Energy Research Scientific Computing Center, a DOE Office of Science User Facility supported by the Office of Science of the U.S. Department of Energy under Contract No. DE-AC02-05CH11231. All the data used to produce the results in this study can be downloaded from https://sbrsfa.velo.pnnl.gov/datasets/?UUID=edde9f0e-9804-4fb5-a048-7ef6185da355.

References

Arntzen, E. V., Geist, D. R., & Dresel, P. E. (2006). Effects of fluctuating river flow on groundwater/surface water mixing in the hyporheic zone of a regulated, large cobble bed river. *River Research and Applications*, *22*(8), 937–946. https://doi.org/10.1002/rra.947

Bao, J., Zhou, T., Huang, M., Hou, Z., Perkins, W., Harding, S., et al. (2018a). Modulating Factors of Hydrologic Exchanges in a Large-Scale River Reach: Insights from Three-Dimensional Computational Fluid Dynamics Simulations. *Hydrological Processes*. https://doi.org/10.1002/hyp.13266

Bao, J., Zhou, T., Huang, M., Hou, Z., Perkins, W., Harding, S., et al. (2018b). Modulating Factors of Hydrologic Exchanges in a Large-Scale River Reach: Insights from Three-Dimensional Computational Fluid Dynamics Simulations. *Hydrological Processes*. https://doi.org/10.1002/hyp.13266

Bencala, K. E., & Walters, R. A. (1983). Simulation of solute transport in a mountain pool-and-riffle stream with a kinetic mass transfer model for sorption. *Water Resources Research*, *19*(3), 732–738. https://doi.org/10.1029/WR019i003p00732

Bloomfield. (2000). *Fourier Analysis of Time Series*.

Boano, F., Camporeale, C., Revelli, R., & Ridolfi, L. (2006). Sinuosity-driven hyporheic exchange in meandering rivers. *Geophysical Research Letters*, *33*(18), L18406. https://doi.org/10.1029/2006GL027630

Boano, F., Harvey, J. W., Marion, a., Packman, a. I., Revelli, R., Ridolfi, L., & Wörman, a. (2014). Hyporheic flow and transport processes: Mechanisms, models, and bioghemical implications. *Reviews of Geophysics*, 1–77. https://doi.org/10.1002/2012RG000417.Received

Cardenas, M. B. (2008). The effect of river bend morphology on flow and timescales of surface water-groundwater exchange across pointbars. *Journal of Hydrology*, *362*(1–2), 134–141. https://doi.org/10.1016/j.jhydrol.2008.08.018

Cardenas, M. B. (2009). A model for lateral hyporheic flow based on valley slope and channel sinuosity. *Water Resources Research*, *45*(1), n/a-n/a. https://doi.org/10.1029/2008WR007442

Cardenas, M. B., Wilson, J. L., & Haggerty, R. (2008). Residence time of bedform-driven hyporheic exchange. *Advances in Water Resources*, *31*(10), 1382–1386. https://doi.org/10.1016/j.advwatres.2008.07.006

Chen, X., Murakami, H., Hahn, M. S., Hammond, G. E., Rockhold, M. L., Zachara, J. M., & Rubin, Y. (2012). Three-dimensional Bayesian geostatistical aquifer characterization at the Hanford 300 Area using tracer test data. *Water Resources Research*, *48*(6), 1–20.

https://doi.org/10.1029/2011WR010675

Chen, X., Hammond, G. E., Murray, C. J., Rockhold, M. L., Vermeul, V. R., & Zachara, J. M. (2013). Application of ensemble-based data assimilation techniques for aquifer characterization using tracer data at Hanford 300 area. *Water Resources Research*, *49*(10), 7064–7076. https://doi.org/10.1002/2012WR013285

Chen, X., Cardenas, M. B., & Chen, L. (2018). Hyporheic Exchange Driven by Three-Dimensional Sandy Bed Forms: Sensitivity to and Prediction from Bed Form Geometry. *Water Resources Research*, *54*(6), 4131–4149. https://doi.org/10.1029/2018WR022663

Coleman, A., Ward, D., Larson, K., & Lettrick, J. (2010). Development of a High-Resolution Bathymetry Dataset for the Columbia River through the Hanford Reach. *Pnnl-19878*, (September).

Cook, P. L. M., Wenzhöfer, F., Rysgaard, S., Galaktionov, O. S., Meysman, F. J. R., Eyre, B. D., et al. (2006). Quantification of denitrification in permeable sediments: Insights from a two-dimensional simulation analysis and experimental data. *Limnology and Oceanography: Methods*, *4*(3), 294–307. https://doi.org/10.4319/lom.2006.4.294

Dwivedi, D., Arora, B., Steefel, C. I., Dafflon, B., & Versteeg, R. (2018). Hot Spots and Hot Moments of Nitrogen in a Riparian Corridor. *Water Resources Research*, *54*(1), 205–222. https://doi.org/10.1002/2017WR022346

Ely, D. M., Burns, E. R., Morgan, D. S., & Vaccaro, J. J. (2014). Numerical Simulation of Groundwater Flow in the Columbia Plateau Regional Aquifer System, Idaho, Oregon, and Washington. *U.S. Geological Survey*, (Scientific Investigations Report 2014-5127), 90. https://doi.org/10.3133/SIR20145127

Freer, J., McDonnell, J. J., Beven, K. J., Peters, N. E., Burns, D. A., Hooper, R. P., et al. (2002). The role of bedrock topography on subsurface storm flow. *Water Resources Research*, *38*(12), 5-1-5–16. https://doi.org/10.1029/2001WR000872

GDAL. (2018). GDAL/OGR Geospatial Data Abstraction software Library. Open Source Geospatial Foundation. URL http://gdal.org.

Gee, G. W., Oostrom, M., Freshley, M. D., Rockhold, M. L., & Zachara, J. M. (2007). Hanford Site Vadose Zone Studies: An Overview. *Vadose Zone Journal*, *6*(4), 899. https://doi.org/10.2136/vzj2006.0179

Gomez-Velez, J. D., & Harvey, J. W. (2014). A hydrogeomorphic river network model predicts where and why hyporheic exchange is important in large basins. *Geophysical Research Letters*, *41*(18), 6403–6412. https://doi.org/10.1002/2014GL061099

Gomez-Velez, J. D., Harvey, J. W., Cardenas, M. B., & Kiel, B. (2015). Denitrification in the Mississippi River network controlled by flow through river bedforms. *Nature Geoscience*, *8*(12), 941–945. https://doi.org/10.1038/ngeo2567

Gomez-Velez, J. D., Wilson, J. L., Cardenas, M. B., & Harvey, J. W. (2017). Flow and Residence Times of Dynamic River Bank Storage and Sinuosity-Driven Hyporheic Exchange. *Water Resources Research*, *53*(10), 8572–8595. https://doi.org/10.1002/2017WR021362

Gu, C., Anderson, W., & Maggi, F. (2012). Riparian biogeochemical hot moments induced by stream fluctuations. *Water Resources Research*, *48*(9), W09546. https://doi.org/10.1029/2011WR011720

Hammond, G. E., & Lichtner, P. C. (2010). Field-scale model for the natural attenuation of uranium at the Hanford 300 Area using high-performance computing. *Water Resources Research*, *46*(9), 1–31. https://doi.org/10.1029/2009WR008819

Hammond, G. E., Lichtner, P. C., & Rockhold, M. L. (2011). Stochastic simulation of uranium migration at the Hanford 300 Area. *Journal of Contaminant Hydrology*, *120–121*(C), 115–128. https://doi.org/10.1016/j.jconhyd.2010.04.005

Hammond, G. E., Lichtner, P. C., & Mills, R. T. (2014). Evaluating the performance of parallel subsurface simulators: An illustrative example with PFLOTRAN. *Water Resources Research*, *50*(1), 208–228. https://doi.org/10.1002/2012WR013483

Hammond, T. B. (2015). *Process for Constructing a Three-dimensional Geological Framework Model of the Hanford Site 100 Area*.

Hartman, M. J. (2016). *Hanford Site groundwater monitoring report for 2016, DOE/RL-2016-67 Revision 0, U.S. Department of Energy, Richland Operations Office, Richland, Washington.*

Harvey, J., & Gooseff, M. (2015). River corridor science: Hydrologic exchange and ecological consequences from bedforms to basins. *Water Resources Research*, *51*(9), 6893–6922. https://doi.org/10.1002/2015WR017617

Hester, E. T. (2014). Controls on mixing-dependent denitrificaiotn in hyporheic zones induced by riverbed dunes: A steady state modeling study. *Water Resources Research*, 1–19. https://doi.org/10.1002/2014WR015424.Received

Heywood, C.E., Kahle, S.C., Olsen, T.D., Patterson, J.D., and Burns, E. (2016). *Simulation of groundwater storage changes in the eastern Pasco Basin, Washington*. https://doi.org/10.3133/sir20165026.

Johnson, T., Versteeg, R., Thomle, J., Hammond, G., Chen, X., & Zachara, J. (2015). Four-dimensional electrical conductivity monitoring of stage-driven river water intrusion: Accounting for water table effects using a transient mesh boundary and conditional inversion constraints. *Water Resources Research*, *51*(8), 6177–6196. https://doi.org/10.1002/2014WR016129

Kasahara, T., & Wondzell, S. M. (2003). Geomorphic controls on hyporheic exchange flow in mountain streams. *Water Resources Research*, *39*(1), SBH 3-1-SBH 3-14. https://doi.org/10.1029/2002WR001386

Kiel, B. A., & Cardenas, M. B. (2014). Lateral hyporheic exchange throughout the Mississippi River network. *Nature Geoscience*, *7*(6), 413–417. https://doi.org/10.1038/ngeo2157

Knights, D., Sawyer, A. H., Barnes, R. T., Musial, C. T., & Bray, S. (2017). Tidal controls on riverbed denitrification along a tidal freshwater zone. *Water Resources Research*, *53*(1), 799–816. https://doi.org/10.1002/2016WR019405

Liu, Y., Liu, C., Kukkadapu, R. K., McKinley, J. P., Zachara, J., Plymale, A. E., et al. (2015). 99Tc(VII) Retardation, Reduction, and Redox Rate Scaling in Naturally Reduced Sediments. *Environmental Science and Technology*, *49*(22), 13403–13412. https://doi.org/10.1021/acs.est.5b03273

Liu, Y., Liu, C., Nelson, W. C., Shi, L., Xu, F., Liu, Y., et al. (2017). Effect of Water Chemistry and Hydrodynamics on Nitrogen Transformation Activity and Microbial Community Functional Potential in Hyporheic Zone Sediment Columns. *Environmental Science & Technology*, acs.est.6b05018. https://doi.org/10.1021/acs.est.6b05018

Ma, R., Liu, C., Greskowiak, J., Prommer, H., Zachara, J., & Zheng, C. (2014). Influence of calcite on uranium(VI) reactive transport in the groundwater-river mixing zone. *Journal of Contaminant Hydrology*, *156*, 27–37. https://doi.org/10.1016/j.jconhyd.2013.10.002

Magliozzi, C., Grabowski, R., Packman, A. I., & Krause, S. (2018). Toward a conceptual framework of hyporheic exchange across spatial scales. *Hydrology and Earth System Sciences Discussions*, (May), 1–37. https://doi.org/10.5194/hess-2018-268

751 Malzone, J. M., Lowry, C. S., & Ward, A. S. (2016). Response of the hyporheic zone to transient
752 groundwater fluctuations on the annual and storm event time scales. *Water Resources*
753 *Research*, *52*(7), 5301–5321. https://doi.org/10.1002/2015WR018056
754 Marzadri, A., Tonina, D., Bellin, A., & Tank, J. L. (2014). A hydrologic model demonstrates
755 nitrous oxide emissions depend on streambed morphology. *Geophysical Research Letters*,
756 *41*(15), 5484–5491. https://doi.org/10.1002/2014GL060732
757 Murphy, E. M., Ginn, T. R., & Phillips, J. L. (1996). Geochemical Estimates of Paleorecharge in
758 the Pasco Basin: Evaluation of the Chloride Mass Balance Technique. *Water Resources*
759 *Research*, *32*(9), 2853–2868. https://doi.org/10.1029/96WR01529
760 Musial, C. T., Sawyer, A. H., Barnes, R. T., Bray, S., & Knights, D. (2016). Surface water-
761 groundwater exchange dynamics in a tidal freshwater zone. *Hydrological Processes*, *30*(5),
762 739–750. https://doi.org/10.1002/hyp.10623
763 Niehus, S. E., Perkins, W. A., & Richmond, M. C. (2014). Simulation of Columbia River
764 Hydrodynamics and Water Temperature from 1917 through 2011 in the Hanford Reach,
765 (September 2014).
766 Richards, L. a. (1931). Capillary Conduction of Liquids Through Porous Mediums. *Physics*,
767 *1*(5), 318. https://doi.org/10.1063/1.1745010
768 Richmond, M. C., & Perkins, W. A. (2009). Efficient calculation of dewatered and entrapped
769 areas using hydrodynamic modeling and GIS. *Environmental Modelling and Software*,
770 *24*(12), 1447–1456. https://doi.org/10.1016/j.envsoft.2009.06.001
771 Rockhold, M. L. (2013). *System-Scale Model of Aquifer, Vadose Zone, and River Interactions*
772 *for the Hanford 300 Area – Application to Uranium Reactive Transport*. *PNNL*.
773 Rockhold, M. L., Fayer, M. J., Kincaid, C. T., & Gee, G. W. (1995). *Estimation of natural*
774 *groundwater recharge for the performance assessment of a low-level waste disposal facility*
775 *at the Hanford Site*.
776 Schmadel, N. M., Ward, A. S., Lowry, C. S., & Malzone, J. M. (2016). Hyporheic exchange
777 controlled by dynamic hydrologic boundary conditions. *Geophysical Research Letters*, 1–
778 10. https://doi.org/10.1002/2016GL068286.Received
779 Shuai, P., Cardenas, M. B., Knappett, P. S. K., Bennett, P. C., & Neilson, B. T. (2017).
780 Denitrification in the banks of fluctuating rivers: The effects of river stage amplitude,
781 sediment hydraulic conductivity and dispersivity, and ambient groundwater flow. *Water*
782 *Resources Research*, Under review. https://doi.org/10.1002/2017WR020610
783 Song, X., Chen, X., Stegen, J., Hammond, G., Song, H.-S., Dai, H., et al. (2018). Drought
784 Conditions Maximize the Impact of High-Frequency Flow Variations on Thermal Regimes
785 and Biogeochemical Function in the Hyporheic Zone. *Water Resources Research*.
786 https://doi.org/10.1029/2018WR022586
787 Stegen, J. C., Fredrickson, J. K., Wilkins, M. J., Konopka, A. E., Nelson, W. C., Arntzen, E. V.,
788 et al. (2016). Groundwater–surface water mixing shifts ecological assembly processes and
789 stimulates organic carbon turnover. *Nature Communications*, *7*, 11237.
790 https://doi.org/10.1038/ncomms11237
791 Stonedahl, S. H., Harvey, J. W., & Packman, A. I. (2013). Interactions between hyporheic flow
792 produced by stream meanders, bars, and dunes. *Water Resources Research*, *49*(9), 5450–
793 5461. https://doi.org/10.1002/wrcr.20400
794 Thorne, P. D. (2004). *Atmospheric Data Package for the 2004 Composite Analysis*.
795 Thorne, P. D., Bergeron, M. P., Williams, M. D., & Freedman, V. L. (2006). *River Data Package*
796 *for Hanford Assessments*. Retrieved from

http://www.pnl.gov/main/publications/external/technical_reports/PNNL-14824rev1.pdf
Tonina, D., & Buffington, J. M. (2007). Hyporheic exchange in gravel bed rivers with pool-riffle morphology: Laboratory experiments and three-dimensional modeling. *Water Resources Research*, *43*(1), 1–16. https://doi.org/10.1029/2005WR004328
Ward, A. S., Gooseff, M. N., & Singha, K. (2013). How does subsurface characterization affect simulations of hyporheic exchange? *GroundWater*, *51*(1), 14–28. https://doi.org/10.1111/j.1745-6584.2012.00911.x
Ward, A. S., Schmadel, N. M., & Wondzell, S. M. (2018). Simulation of dynamic expansion, contraction, and connectivity in a mountain stream network. *Advances in Water Resources*, *114*, 64–82. https://doi.org/10.1016/j.advwatres.2018.01.018
Williams, M. (2008). *Three-Dimensional Groundwater Models of the 300 Area at the Hanford Site , Washington State*. *PNNL*. https://doi.org/10.2172/969184
Yabusaki, S. B., Fang, Y., & Waichler, S. R. (2008). Building conceptual models of field-scale uranium reactive transport in a dynamic vadose zone-aquifer-river system. *Water Resources Research*, *44*(12). https://doi.org/10.1029/2007WR006617
Yang, C., Zhang, Y.-K., Liu, Y., Yang, X., & Liu, C. (2018). Model-Based Analysis of the Effects of Dam-Induced River Water and Groundwater Interactions On Hydro-Biogeochemical Transformation of Redox Sensitive Contaminants in a Hyporheic Zone. *Water Resources Research*. https://doi.org/10.1029/2018WR023286
Zachara, J. M., Long, P. E., Bargar, J., Davis, J. A., Fox, P., Fredrickson, J. K., et al. (2013). Persistence of uranium groundwater plumes: Contrasting mechanisms at two DOE sites in the groundwater-river interaction zone. *Journal of Contaminant Hydrology*, *147*, 45–72. https://doi.org/10.1016/j.jconhyd.2013.02.001
Zachara, J. M., Chen, X., Murray, C., & Hammond, G. (2016). River stage influences on uranium transport in a hydrologically dynamic groundwater-surface water transition zone. *Water Resources Research*, *52*(3), 1568–1590. https://doi.org/10.1002/2015WR018009
Zarnetske, J. P., Haggerty, R., Wondzell, S. M., & Baker, M. A. (2011). Dynamics of nitrate production and removal as a function of residence time in the hyporheic zone. *Journal of Geophysical Research*, *116*(G1), G01025. https://doi.org/10.1029/2010JG001356
Zarnetske, J. P., Haggerty, R., Wondzell, S. M., Bokil, V. a., & González-Pinzón, R. (2012). Coupled transport and reaction kinetics control the nitrate source-sink function of hyporheic zones. *Water Resources Research*, *48*(11), 1–15. https://doi.org/10.1029/2012WR011894
Zhou, T., Bao, J., Huang, M., Hou, Z., Arntzen, E., Song, X., et al. (2018). Riverbed Hydrologic Exchange Dynamics in a Large Regulated River Reach. *Water Resources Research*, 2715–2730. https://doi.org/10.1002/2017WR020508

836 Figure 1. (a) Study site showing the Hanford Reach and Columbia River bathymetry. Hanford Site boundary is
837 outlined with gray line. Former operational areas at the Hanford site are labeled on the map. (b) 3-D
838 representation of land surface topography within the model domain. (c) Hourly river stages along the reach
839 (gray) simulated by MASS1, with highlighted locations at upstream (red), midstream (black) and downstream
840 (blue) as indicated in panel (a).
841 Figure 2. Thickness of Hanford unit within the model domain. The dashed lines (black) are the cross-sectional
842 locations of river segment. Also shown is a paleochannel formed by glacial floods.
843 Figure 3. (a) Model domain showing various geologic layers. (b) Cross-section showing model layers
844 Figure 4. (a) River stages during year 2011 at midstream location; (b) groundwater table contour at high and low
845 river stages, with white arrows indicating the flow directions; (c) river tracer plume along the reach at high and
846 low river stages; and (d) Enlarged river tracer plume near the horn area.
847 Figure 5. (a) River stages at midstream location (~ 40 km from downstream end) during simulation period from
848 2011 to 2015. (b) Heat map showing the spatial (vertical axis, where 0=downstream end of the Hanford Reach
849 and 75=tailrace of Priest Rapids Dam) and temporal (horizontal axis) patterns of HEFs. (c) Average Hanford
850 Formation thickness across the river reach. (d) Two snapshots of HEFs across the riverbed at high and low river
851 stages.
852 Figure 6. (a) Numbered river segments along the Hanford Reach. (b) Relationship between exchange flux per river
853 channel length and river channel sinuosity. (c) Relationship between exchange flux per river channel length and
854 the average thickness of Hanford Formation sediment below the riverbed. Also shown are the linear regression
855 lines (red) and R-squared values.
856 Figure 7. (a-j) 2-D cross-sections showing the extent of river tracer plume overlying geologic units. Note that
857 geologic unit color scheme is the same with Figure 3 but with 80% transparency to allow the demonstration of
858 tracer plumes.
859 Figure 8. Spectral analysis for two river boundary conditions at midstream location using FFT. (a) River stage time
860 series under both cases. (b) Spectral analysis for river stage under both cases. (c) Exchange flux time series
861 under both cases. (d) Spectral analysis for exchange flux under both cases.
862 Figure 9. (a) River stage for weekly smoothed case at midstream location. (b) Heat map showing temporal-spatial
863 distribution of exchange flux across the riverbed. (c) Average thickness of Hanford Formation across the river
864 reach.
865 Figure 10. (a) River stage over the simulation period under both cases. (b) Histograms of HEFs in both cases. (c)
866 Scatter plot between flux rates under both cases. Red and blue circles correspond to the red and blue fluxes in
867 panel (d). Also shown is the one-to-one line (black). (d) Heat map showing changes in HEF directions. River
868 switched from gaining to losing (blue) and from losing to gaining (red).
869 Figure 11. Annual river gaining, losing, net and total exchange volume under both cases. Note the scale difference
870 for Vnet.
871 Figure 12. (a) Simulated river tracer plume (b) Chromium plumes (c) Tritium plume and (d) Nitrate plume at
872 Hanford horn areas in year 2010.
873
874
875 Table 1. Hydrogeologic properties of geologic units
876 Table 2. ANOVA summary table for exchange flux against sinuosity and thickness of Hanford Formation
877

Water Resources Research

Supporting Information for

Daily Dam Operations and Subsurface Hydrogeology Control Hydrologic Exchange Flows Hot Spots and Hot Moments in a Regulated River Reach

Pin Shuai[1], Xingyuan Chen[1], Xuehang Song[1], Glenn E. Hammond[2], John Zachara[1], Patrick Royer[1], Huiying Ren[1], William A. Perkins[1], Marshall C. Richmond[1], and Maoyi Huang

[1]Pacific Northwest National Laboratory, Richland, Washington, USA

[2]Sandia National Laboratories, Albuquerque, New Mexico, USA

Contents of this file

Figures S1 to S5

Additional Supporting Information (Files uploaded separately)

Movie S1. Animation of groundwater level contour over the simulation period from 2011 to 2015.
Movie S2. Animation of river water tracer plumes over the simulation period from 2011 to 2015.
Movie S3. Animation of exchange flux across the riverbed for the entire reach over the simulation period from 2011 to 2015.

Introduction

The supporting information provides the supplementary figures referenced in the main article. Figure S3-S5 provides the comparison of observed and simulated data including groundwater levels and specific conductance at selected wells. Please note those selected wells are not all inclusive, and many wells do not have continuous monitoring data and thus are not included here. For more well information, please go to http://phoenix.pnnl.gov or https://www.hanford.gov/page.cfm/SoilGroundwaterAnnualReports.

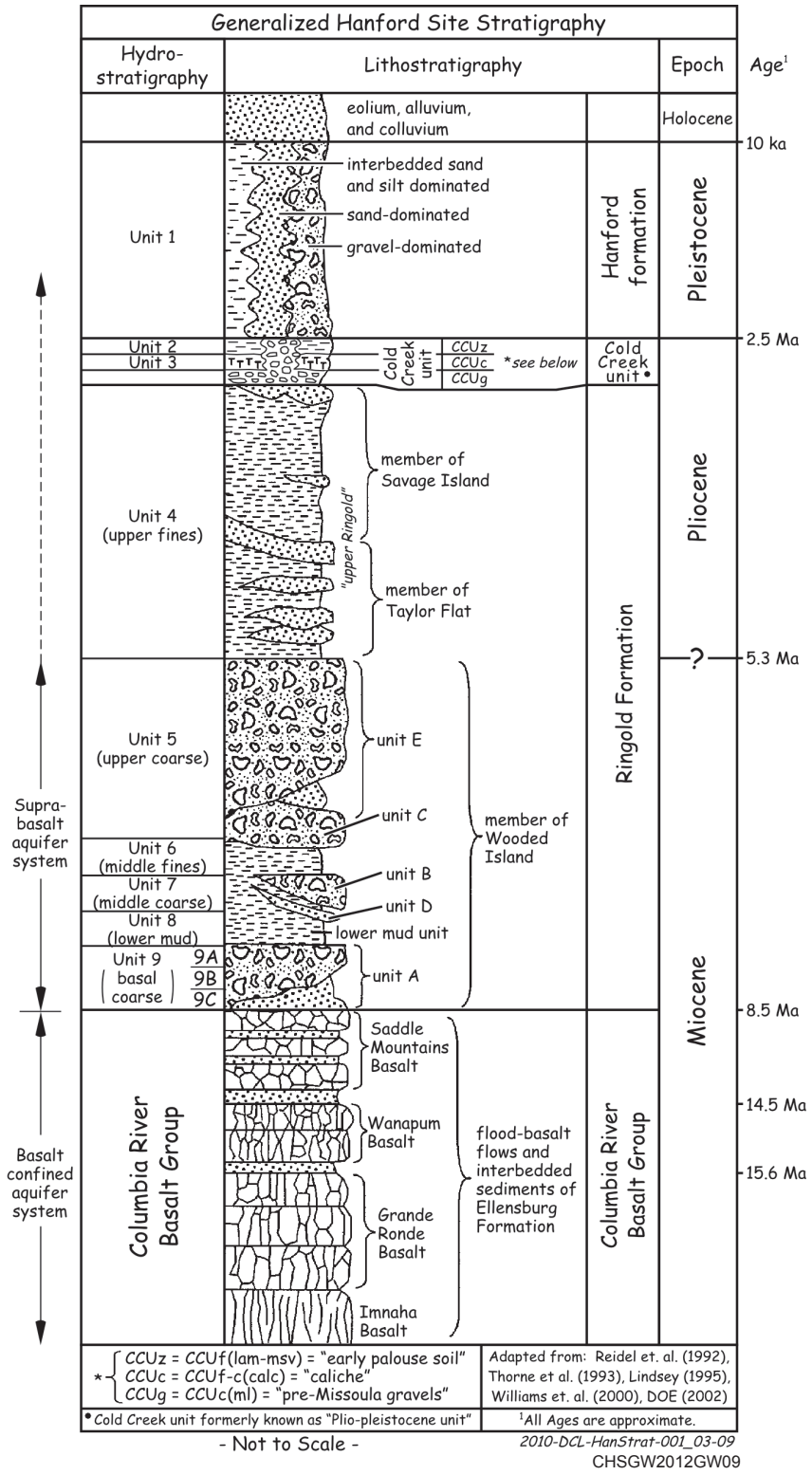

Figure S1. Generalized Hanford stratigraphy (from Hartman, 2016)

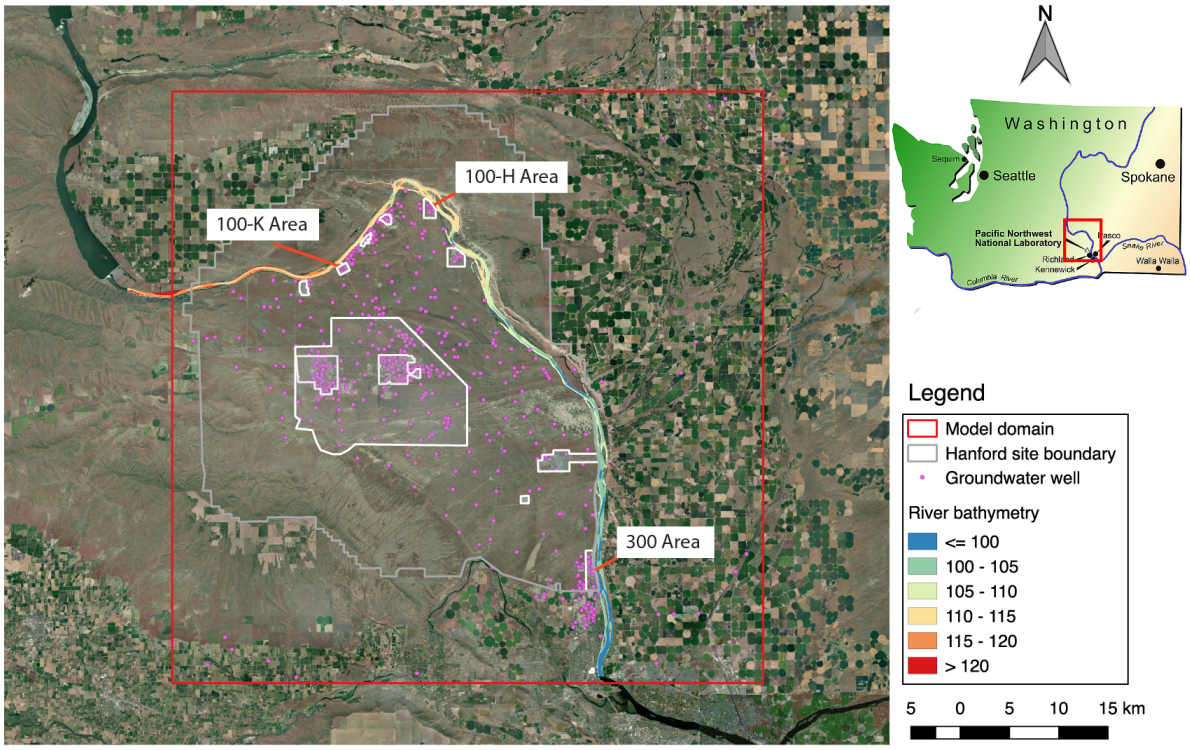

Figure S2. Study site showing Hanford Areas. Modified from Figure 1 in the manuscript.

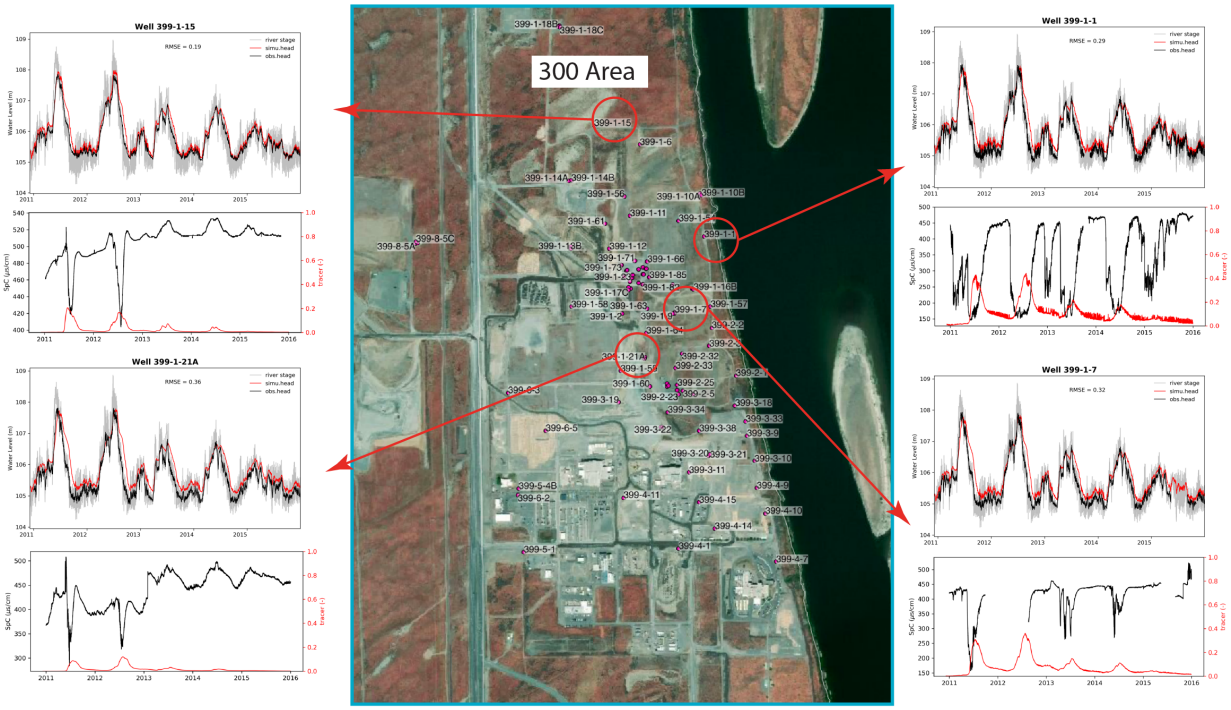

Figure S3. Selected groundwater monitoring wells showing observed versus simulated groundwater table and observed specific conductivity versus simulated river tracer concentration in 300 Area.

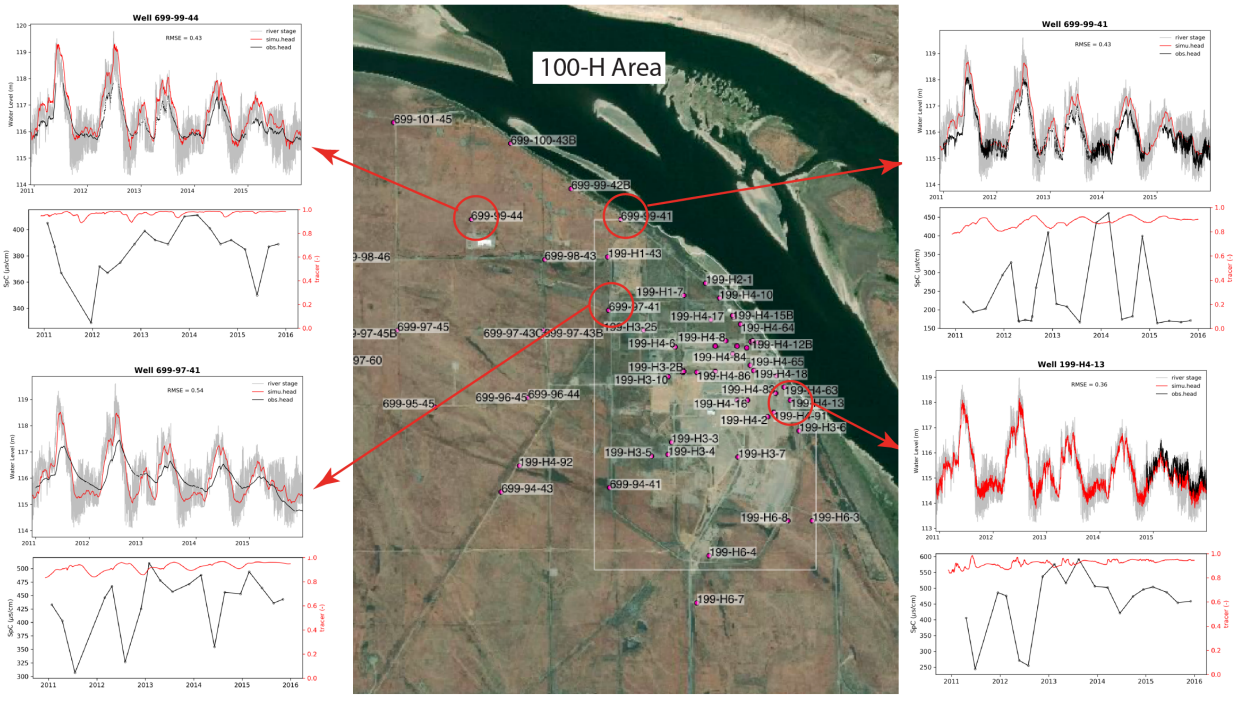

Figure S4. Selected groundwater monitoring wells showing observed versus simulated groundwater table and observed specific conductivity versus simulated river tracer concentration in 100-H Area.

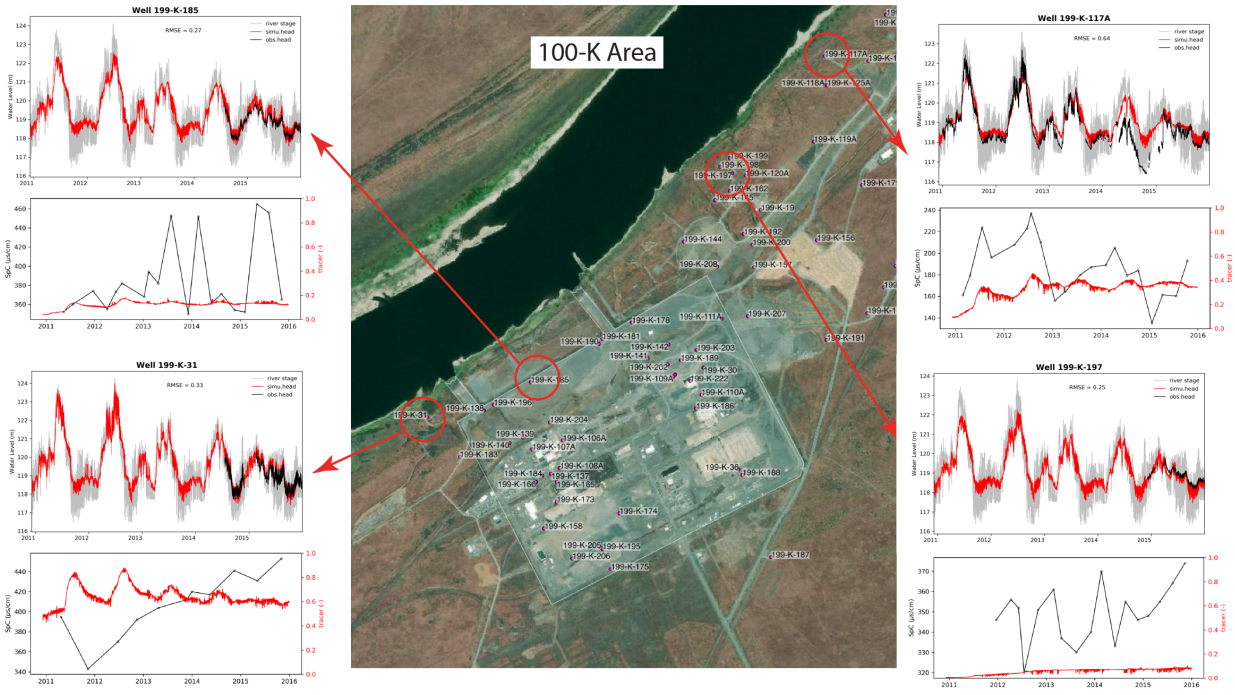

Figure S5. Selected groundwater monitoring wells showing observed versus simulated groundwater table and observed specific conductivity versus simulated river tracer concentration in 100-K Area.

Movie S1. Animation of groundwater level contour over the simulation period from 2011 to 2015.
Movie S2. Animation of river water tracer plumes over the simulation period from 2011 to 2015.
Movie S3. Animation of exchange flux across the riverbed for the entire reach over the simulation period from 2011 to 2015.